Control of meiotic entry by dual inhibition of a key mitotic transcription factor

Amanda J. Su[1], Siri C. Yendluri[1] and Elçin Ünal[1, §]

[1] Department of Molecular and Cell Biology, University of California, Berkeley, CA, United States, 94720

[§] Lead contact: elcin@berkeley.edu

Keywords: meiosis, mitosis, transcription, cell cycle, LUTI, uORF, Ime1, Swi4, SBF, Whi5, Rb, E2F

Abbreviations: SBF (Swi4/6 cell cycle box [SCB] Binding Factor); MBF (Mlu1 cell cycle box [MCB] Binding Factor); LUTI (Long Undecoded Transcript Isoform); TF (Transcription Factor)

HIGHLIGHTS

- SBF subunit Swi4 is downregulated at meiotic entry by the LUTI-based mechanism
- *SWI4*^{LUTI} and Whi5 work together to inhibit SBF at meiotic entry
- SBF and Ime1 TFs antagonize each other, ensuring mutually exclusive cell states
- SBF-target G1 cyclins block meiosis by preventing Ime1-Ume6 interaction

SUMMARY

The mitosis to meiosis transition requires dynamic changes in gene expression, but whether and how the mitotic transcriptional machinery is regulated during this transition is unknown. In budding yeast, SBF and MBF transcription factors initiate the mitotic gene expression program. Here, we report two mechanisms that work together to restrict SBF activity during meiotic entry: repression of the SBF-specific Swi4 subunit through LUTI-based regulation and inhibition of SBF by Whi5, a homolog of the Rb tumor suppressor. We find that untimely SBF activation causes downregulation of early meiotic genes and delays meiotic entry. These defects are largely driven by the SBF-target G1 cyclins, which block the interaction between the central meiotic regulator Ime1 and its cofactor Ume6. Our study provides insight into the role of *SWI4*^{LUTI} in establishing the meiotic transcriptional program and demonstrates how the LUTI-based regulation is integrated into a larger regulatory network to ensure timely SBF activity.

INTRODUCTION

A key aspect in understanding developmental programs and cell state transitions is mapping the interplay between transcription factors and their associated gene regulatory networks. In the budding yeast *Saccharomyces cerevisiae*, the transition from mitotic growth to meiotic differentiation is a crucial decision that is regulated by multiple inputs, such as nutrient availability, respiration competence, and cell identity. Under nutrient-limiting conditions, a diploid cell enters the meiotic program to produce four haploid gametes. The process of meiotic entry is tightly controlled by the master transcriptional regulator Ime1, as both extrinsic (e.g. nutrient status, extracellular pH) and intrinsic (e.g. mating type, mitochondrial function) cues are integrated at the *IME1* promoter (Kassir et

al., 1988; Honigberg, 2003; reviewed in van Werven and Amon, 2011). Once translated, Ime1 is phosphorylated by the Rim11 and Rim15 kinases to promote its nuclear localization and interaction with Ume6 (Vidan and Mitchell, 1997; Pnueli et al., 2004; Malathi et al., 1999, 1997). In mitotically dividing cells, Ime1 target genes are repressed by Ume6 through its association with the Sin3-Rpd3 histone deacetylase complex (Kardosh and Struhl, 1997; Rundlett E. et al., 2003). However, under nutrient starvation, entry into the meiotic program is initiated by the interaction between Ime1 and Ume6, which together function as a transcriptional activator, culminating in the induction of early meiotic genes (Bowdish et al., 1995). Mitosis to meiosis transition requires dynamic remodeling of the gene regulatory networks to maintain the mutual exclusivity of these programs. While entry into the mitotic program is initiated by the central transcription factors SBF and MBF (Spellman et al., 1998; Iyer et al., 2001), whether and how these complexes are regulated during meiotic entry is unknown.

The molecular mechanisms regulating entry into the mitotic cell cycle, also known as G1/S transition, are functionally conserved from yeast to metazoans (reviewed in Van Den Heuvel and Dyson, 2008). SBF and MBF are heterodimeric transcription factors composed of Swi4-Swi6 and Mbp1-Swi6 subunits, respectively (Figure 1A). These transcription factors are homologous to the mammalian E2Fs. E2Fs are negatively regulated by the tumor suppressor protein Rb, which is homologous to the budding yeast Whi5 that inhibits SBF in early G1 (De Bruin et al., 2004; Costanzo et al., 2004; Hasan et al., 2014). Whi5-based SBF inhibition is relieved by cyclin/CDK-dependent phosphorylation and subsequent re-localization of Whi5 from the nucleus to the

74 cytoplasm (Wagner et al., 2009). Although SBF and MBF act in parallel during the G1/S
75 transition (Spellman et al., 1998; Iyer et al., 2001), they activate functionally specialized
76 subsets of gene targets. SBF regulates the expression of genes involved in budding and
77 cell morphogenesis, while MBF-regulated genes are involved in DNA replication and
78 repair (Iyer et al., 2001; Simon et al., 2001). Despite the well-characterized function in
79 budding yeast mitotic growth, the regulation and function of SBF and MBF during meiotic
80 entry remains largely unknown. In contrast to mitotic divisions where budding and DNA
81 replication occur simultaneously, the meiotic program requires DNA replication and
82 repair, but not bud morphogenesis or asymmetric growth. Accordingly, the regulation and
83 subsequent activity of SBF and MBF are likely to be divergent to establish meiotic entry.
84
85 The activity of SBF and MBF is regulated in part through subunit abundance, which in
86 turn controls expression of the G1/S regulon (Dorsey et al., 2018). For example,
87 overexpression of a hyperactive allele of *SWI4* can trigger premature entry into the cell
88 cycle (Sidorova and Breeden, 2002). Additionally, *SWI4* has also been shown to be
89 haploinsufficient and rate limiting during G1/S progression (Mcinerny et al., 1997). These
90 results suggest that the precise levels of SBF and MBF subunits are important for
91 activating the G1/S regulon at the correct time.
92
93 Three key observations support differential regulation of SBF and MBF during the meiotic
94 program: First, a meiotic mass spectrometry dataset suggests that Swi4 has dynamic
95 protein behavior, which is not observed for its counterparts Swi6 and Mbp1 (Cheng et al.,
96 2018). Second, meiotic cells express a repressive non-canonical mRNA from the *SWI4*

97 locus called LUTI (Brar et al., 2012; Tresenrider et al., 2021), which stands for Long
98 Undecoded Transcript Isoform (Chen et al., 2017; Chia et al., 2017). Third, two SBF-
99 specific targets, namely the G1-cyclins *CLN1* and *CLN2*, have been shown to repress
100 early meiotic gene expression (Colomina et al., 1999).
101
102 LUTI-based gene regulation repurposes gene-activating transcription factors as
103 repressors by a two-pronged mechanism (Chen et al., 2017; Chia et al., 2017; Tresenrider
104 and Ünal, 2017; Tresenrider et al., 2021). First, transcription factor-dependent activation
105 of the distal LUTI promoter results in co-transcriptional silencing of the downstream
106 canonical gene promoter. Second, the coding sequence (CDS) within the LUTI is
107 translationally repressed due to competitive translation of the upstream open reading
108 frames (uORFs) in the LUTI-specific 5′ leader. Consequently, upregulation of the LUTI
109 results in downregulation of the canonical mRNA and corresponding protein. While LUTIs
110 are conserved from yeast to humans and have been identified in different cellular contexts
111 (Cheng et al., 2018; Van Dalfsen et al., 2018; Hollerer et al., 2019; Jorgensen et al., 2020),
112 their biological significance remains poorly understood. In fact, only a single LUTI has
113 been assigned a biological role so far with distinct phenotypic outcomes resulting from its
114 loss or gain of function (Chen et al., 2017; Chia et al., 2017).
115
116 In this study, we aimed to investigate the differential regulation of SBF and MBF during
117 the meiotic program and determine how the untimely activation of SBF impacts meiotic
118 entry. We found that overexpression of Swi4 results in the activation of SBF targets and
119 concomitant downregulation of the early meiotic genes. SBF targets Cln1 and Cln2 inhibit

120 meiotic entry by blocking the interaction between Ime1 and its cofactor Ume6.
121 Furthermore, the LUTI-based mechanism causes downregulation of Swi4 protein
122 synthesis and acts in conjunction with Whi5 to restrict SBF activity during meiosis.
123 Overall, our study reveals the functional role of a LUTI in establishing the early meiotic
124 transcriptome, demonstrates how the LUTI-based regulation is integrated into a larger
125 regulatory network to ensure timely SBF activity, and provides mechanistic insights into
126 how SBF misregulation impedes transition from mitotic to meiotic cell fate.
127

128 **RESULTS**

129 **Swi4 is the sole downregulated subunit within the SBF and MBF complexes during**
130 **meiosis**

131 While the SBF and MBF transcription factors have been heavily studied in the context of
132 the mitotic cell cycle, their involvement in regulating the meiotic transcriptional program is
133 not well understood. To understand the regulation and function of these complexes during
134 meiosis, we first monitored the levels of SBF and MBF subunits throughout a meiotic time
135 course. Cells were first grown in rich media overnight and were then transferred to pre-
136 sporulation media. After additional overnight growth, cells were shifted to sporulation
137 media (SPO) to induce meiosis, and samples were taken hourly for protein extraction and
138 immunoblotting to monitor the abundance of each subunit. Unlike the mitotic G1/S
139 transition (Kelliher et al., 2018), meiotic entry resulted in ~30% decrease in Swi4 levels
140 after 2 hours, while Mbp1 and Swi6 levels were increased (Figure 1B and 1C*).* These
141 data indicate that Swi4 is the sole subunit within SBF and MBF whose level declines

142 during meiotic entry and are consistent with a published mass spectrometry dataset
143 (Cheng et al., 2018).
144
145 We next examined the expression of a set of well-characterized transcripts that are
146 regulated by SBF or MBF (Iyer et al., 2001; Simon et al., 2001; Bean et al., 2005; Harris
147 et al., 2013; Smolka et al., 2012) using a published meiotic RNA-seq dataset (Brar et al.,
148 2012). This analysis revealed that compared to mitotically dividing cells, most of the SBF-
149 specific target genes had either low or no expression during early meiosis (Figure 1D). In
150 contrast, most of the MBF targets displayed increased expression upon meiotic entry
151 (Figure 1D).
152
153 Based on our findings thus far, we propose that Swi4 levels are tightly regulated in meiosis
154 to ensure that SBF targets, including *CLN1* and *CLN2*, are turned off during meiotic entry.
155 If Swi4 is indeed limiting for meiotic SBF activity, then higher Swi4 levels should lead to
156 increased expression of SBF targets. To test this possibility, we overexpressed *SWI4* by
157 placing it under the regulation of the *ATG8* promoter (*pATG8-SWI4*), which is highly
158 expressed in meiosis (Brar et al., 2012). The steady-state level of *pATG8*-driven Swi4
159 was 5 times higher than wild type (Figure S1A and S1B). Using reverse transcription
160 coupled with quantitative polymerase chain reaction (RT-qPCR), we measured the
161 transcript levels of well-characterized SBF targets and observed a significant increase in
162 the expression of *CLN1* and *CLN2* in *pATG8-SWI4* cells relative to wild type (Figure 1E,
163 $p = 0.0351$ [*CLN1*], $p = 0.0013$ [*CLN2*], two-tailed t-test). In contrast, the MBF-specific
164 targets *CDC21* and *RNR1* remained similar (Figure 1E, $p = 0.8488$ [*CDC21*], $p = 0.0859$

165 [*RNR1*], two-tailed t-test). These findings indicate that upregulation of *SWI4* is sufficient
166 to induce the expression of SBF-specific targets *CLN1* and *CLN2* in meiosis without
167 affecting MBF-specific targets.
168
169 To test whether the downregulation of *SWI4* is functionally important for meiotic
170 progression, we used time-lapse fluorescence microscopy and visualized the kinetics of
171 meiotic divisions in *pATG8-SWI4* cells relative to wild type. By tracking the endogenous
172 histone H2B fused to the red fluorescent protein mCherry (Htb1-mCherry), we found that
173 *SWI4* overexpression caused a significant delay in meiotic progression (Figure 1F, $p =$
174 0.0045, Mann-Whitney test). We conclude that downregulation of *SWI4* is necessary for
175 timely meiotic progression.
176
177 **Regulation of Swi4 abundance is required for timely meiotic entry**
178 Since Swi4 abundance, and by inference SBF activity, was decreased during the mitosis-
179 to-meiosis transition, we hypothesized that the meiotic progression delay observed in
180 *pATG8-SWI4* cells was due to meiotic entry defects. To test this we monitored Ime1, a
181 meiosis-specific transcription factor and a master regulator of meiotic entry (Kassir et al.,
182 1988; Honigberg, 2003; reviewed in van Werven and Amon, 2011). To quantify the bulk
183 levels of Ime1 protein in meiosis, we performed immunoblotting. During meiotic entry (2
184 h in SPO), when Swi4 abundance was elevated, there was a 50% reduction in Ime1 levels
185 in *pATG8-SWI4* cells compared to wild type (Figure S1C and S1D). In parallel, we
186 monitored meiotic entry on a single-cell basis by measuring the localization of
187 endogenous Ime1 carrying an N-terminal green fluorescent protein tag (*GFP-IME1*;

188 Moretto 2018) and Htb1-mCherry. Compared to wild type where > 90% of the cells had
189 nuclear Ime1 following meiotic entry (2 h in SPO), only ~50% of *pATG8-SWI4* cells had
190 nuclear Ime1, which was significantly lower (Figure 2A and 2B, $p = 0.0169$, two-tailed t-
191 test).
192
193 Given that the increase in Swi4 levels coincided with a decrease in Ime1 protein
194 expression and nuclear localization, this raised the possibility that Swi4 interferes with
195 Ime1 function. To further investigate the relationship between these two transcription
196 factors at a single-cell level, we generated strains carrying endogenous fluorescent
197 protein tags for each transcription factor (*GFP-IME1, SWI4-mCherry*). Using DAPI as a
198 nuclear marker, we measured the mean nuclear intensity of each transcription factor
199 before (0 h) and after meiotic entry (4 h) (see Materials and Methods for details on image
200 quantification). In wild type, most cells exhibited decreased nuclear Swi4 and increased
201 nuclear Ime1 upon meiotic entry (Figure 2C-E). Conversely, in the *pATG8-SWI4* mutant,
202 there was a significant shift in the fraction of cells with higher nuclear Swi4 levels (Figure
203 2D and 2E, $p < 0.0001$, Mann-Whitney test,). Additionally, the cells with increased nuclear
204 Swi4 had reduced levels of nuclear Ime1 (Figure 2E, $p < 0.0001$, Mann-Whitney test).
205 This inverse relationship between Swi4 and Ime1 nuclear localization further indicates
206 that higher levels of Swi4 are antagonistic to Ime1 function.
207
208 Ime1 is necessary for the expression of early meiotic genes. Therefore, we next
209 characterized the changes in the early meiotic transcriptome upon *SWI4* overexpression
210 by mRNA-sequencing (mRNA-seq). Using DESeq2 (Love et al., 2014), we identified

211 differentially expressed genes in *pATG8-SWI4* mutant compared to wild type during
212 meiotic entry (2 h in SPO). To investigate general pathways being affected by increased
213 Swi4 levels in meiosis, we ran gene ontology analysis of statistically significant (padj <
214 0.05) output from DESeq2, which revealed that the genes with significantly increased
215 expression were involved in mitosis while those with significantly decreased expression
216 were involved in meiotic processes (Figure S2A and S2B). Regarding the SBF targets,
217 we noticed increased expression of many genes, including *CLN1* and *CLN2* (Figure 2F,
218 Supplemental Table 1). We focused on a cluster of previously identified early meiotic
219 genes involved in DNA replication and recombination (Brar et al., 2012) and observed
220 that more than 50% had a significant decrease in their expression upon *SWI4*
221 overexpression (padj < 0.05, Figure 2F, Supplemental Table 1). Finally, gene set
222 enrichment analysis was performed to test whether expression of either the early meiotic
223 gene set or SBF target gene set is enriched in wild type or *pATG-SWI4* mutant cells
224 (Subramanian et al., 2005). This gene set level analysis revealed significant enrichment
225 of SBF target gene expression (NES = 2.88, p < 0.001, Figure 2G), as well as significant
226 disenrichment of early meiotic gene expression (NES = -2.88, p < 0.001, Figure 2G) in
227 the *pATG8-SWI4* mutant. Altogether, these findings demonstrate that the increased levels
228 of Swi4 during transition from mitotic to meiotic cell fate abruptly activates SBF and
229 disrupts the early meiotic transcriptome, highlighting the importance of *SWI4* regulation.
230
231 As an orthogonal approach, we performed live-cell imaging of Rec8, endogenously
232 tagged with GFP (Rec8-GFP), which is a meiosis-specific cohesin subunit and a direct
233 transcriptional target of Ime1 (Primig et al., 2000; Klein et al., 1999). Htb1-mCherry was

234 used as a nuclear marker. This analysis revealed a significant delay in Rec8-GFP nuclear
235 appearance in the *pATG8-SWI4* strain compared to wild type (Figure 2H and 2I, p =
236 0.0005, Mann-Whitney test). Furthermore, sporulation efficiency was decreased by ~20%
237 in the *pATG8-SWI4* strain relative to wild type (Supplemental Table 2). These findings
238 are consistent with the mRNA-seq data and further underscore the importance of *SWI4*
239 downregulation in establishing a robust meiotic cell fate.
240

241 **Removal of the SBF targets Cln1 or Cln2 partially rescues the meiotic entry delay**
242 **in *pATG8-SWI4* mutants**

243 Overexpression of the G1 cyclins *CLN1*, *CLN2* and *CLN3* has been previously shown to
244 inhibit meiotic entry (Colomina et al., 1999). Given that *CLN1* and *CLN2* are
245 transcriptional targets of SBF, we next determined whether the meiotic progression delay
246 in *pATG8-SWI4* cells could be due to increased G1 cyclin protein levels. We first
247 examined Cln1 and Cln2 protein levels using epitope-tagged alleles at their endogenous
248 loci (*CLN1-3V5* or *CLN2-3V5*) in wild-type and *pATG8-SWI4* cells. In response to *SWI4*
249 overexpression, we observed up to 2-fold and 10-fold increase in Cln1 and Cln2 protein
250 levels, respectively, corroborating the mRNA-seq data (Figure 3A-D).
251

252 To determine whether these two G1 cyclins are functionally responsible for the meiotic
253 progression delay observed in response to SBF misregulation, we performed time-lapse
254 fluorescence microscopy in cells carrying Rec8-GFP and Htb1-mCherry. We found that
255 deletion of either *CLN1* or *CLN2* significantly rescued the meiotic progression delay in the
256 *pATG8-SWI4* mutant (p = 0.0111 [*cln1*Δ], p = 0.0478 [*cln2*Δ], Mann-Whitney test).

257 However, the progression was still delayed compared to wild type, suggesting
258 redundancy (Figure 3E and 3F). We were unable to examine meiotic progression in the
259 *cln1Δ cln2Δ* double mutant due to its severe sickness in the SK1 background.
260 Nevertheless, our analyses establish a causal link demonstrating that both *CLN1* and
261 *CLN2* contribute to the meiotic defects arising from SBF misregulation.
262
263 **Tethering of Ime1 to Ume6 is sufficient to overcome the meiotic block exerted by**
264 **G1 cyclin overexpression**
265 Given the partial rescue of the meiotic delay in *pATG8-SWI4* mutants by the deletion of
266 individual G1 cyclins, we next investigated how the G1 cyclins interfere with meiosis. To
267 this end, we generated transgenes that expressed either *CLN1* or *CLN2* under the control
268 of the *pATG8* promoter for meiotic overexpression. While wild-type cells successfully
269 completed meiosis with more than 94% sporulation efficiency, *CLN2* overexpression
270 resulted in only 8.5% of cells forming gametes. Overexpression of *CLN1* also resulted in
271 a meiotic defect, albeit to a lesser extent than the *pATG8-CLN2* mutant (65% sporulation
272 efficiency, Figure 4A).
273
274 Since the meiotic defect was more pronounced in response to *CLN2* overexpression, we
275 decided to use the *pATG8-CLN2* mutant to explore how G1 cyclins counteract meiosis.
276 To assess meiotic entry, we performed fixed-cell imaging for GFP-Ime1 and found that
277 when *CLN2* was overexpressed, only 5% of the *pATG8-CLN2* cells displayed nuclear
278 GFP-Ime1 signal during early meiosis as opposed to >84% of wild-type cells (Figure 4B
279 and 4C, 2 h in SPO). In parallel, we measured *IME1* transcript and Ime1 protein levels.

280 In both cases, we observed ~30% decrease in abundance in the *pATG8-CLN2* mutant
281 relative to wild type (Figure S4A-C, 2 h in SPO). These data raise the possibility that the
282 meiotic entry defect observed in the *pATG8-CLN2* mutant arises from downregulation of
283 *IME1* expression.
284
285 To test whether the increased levels of Ime1 can rescue the meiotic defect of *pATG8-*
286 *CLN2* mutant, we replaced the endogenous *IME1* promoter with a copper-inducible *CUP1*
287 promoter (Figure 4D). We adapted a previously well-characterized overexpression allele
288 of *IME1*, *pCUP1-IME1,* (Berchowitz et al., 2013; Chia and van Werven, 2016) and
289 included a functional, N-terminal GFP tag to track Ime1's subcellular localization *(pCUP1-*
290 *GFP-IME1*). Use of the *CUP1* promoter was successful in elevating *IME1* transcript and
291 protein levels in the presence of *CLN2* overexpression (Figure S4D-F). Despite the
292 rescue of *IME1* expression, gamete formation was still severely perturbed (Figure 4A).
293 Using a single z-slice to measure mean nuclear intensity, we noticed that the intensity of
294 the nuclear Ime1 signal was significantly lower in the *pATG8-CLN2; pCUP1-GFP-IME1*
295 cells compared to the *pCUP1-GFP-IME1* control (Figure 4E and 4F, $p < 0.0001$, Mann-
296 Whitney test). This finding indicates that rescue of *IME1* expression did not also rescue
297 sporulation, further suggesting a defect in Ime1 nuclear localization. To test this
298 possibility, we utilized a nanobody trap strategy (Fridy et al., 2014) where we C-terminally
299 fused a single-domain anti-GFP antibody to Pus1, a constitutively nuclear localized
300 protein (*PUS1-αGFP*, Figure 4G). In this background, control strains carrying a *GFP-IME1*
301 allele sporulated efficiently, demonstrating that tethering of Ime1 to Pus1 does not
302 interfere with Ime1 function (Figure 4A). Furthermore, mean nuclear intensity of GFP-

303 Ime1 was indistinguishable between *PUS1-αGFP* and *pATG8-CLN2; PUS1-αGFP*,
304 indicating that nuclear localization was fully rescued (Figure 4H and 4I, p = 0.6563 [*PUS1-*
305 *αGFP* vs. *pATG8-CLN2; PUS1-αGFP*], Mann-Whitney test). Surprisingly, these cells still
306 failed to undergo meiosis (Figure 4A), suggesting that G1 cyclins interfere with Ime1
307 function at an additional step beyond misregulating its expression and localization.
308 Alternatively, G1 cyclins could disrupt a different meiotic factor in addition to Ime1.
309
310 To induce early meiotic genes, Ime1 must interact with another transcription factor called
311 Ume6 (Rubin-Bejerano et al., 1996). Since Ime1 itself does not possess a DNA-binding
312 domain, its binding to Ume6 is essential for targeting Ime1 to early meiotic gene
313 promoters (Smith et al., 1993; Rubin-Bejerano et al., 1996). To address whether the G1
314 cyclins might disrupt the interaction between Ime1 and Ume6, we fused the anti-GFP
315 nanobody to Ume6 (*UME6-αGFP*) in the *pATG8-CLN2* strain carrying a GFP tagged Ime1
316 (Figure 4J). This nanobody trap should lead to constitutive tethering of Ime1 to Ume6, as
317 evidenced by the rescue of Ime1 nuclear localization (Figure 4K and 4L, p = 0.035 [wild
318 type vs. *pATG8-CLN2 UME6-αGFP*] Mann-Whitney test). Under these conditions, the
319 sporulation defect of *pATG8-CLN2* mutant was rescued, reaching similar levels to wild
320 type (Figure 4A). Since *IME1* is expressed from its endogenous promoter in the *pATG8-*
321 *CLN2; UME6-αGFP* strain, these data suggest that overexpression of G1 cyclins results
322 in meiotic failure due to reduced Ime1-Ume6 interaction.
323
324 Our findings thus far highlight the biological significance of restricting SBF activity during
325 the transition from mitotic to meiotic cell fate. By downregulating the limiting Swi4 subunit,

326 cells ensure that the SBF regulon is turned off under conditions that favor meiotic entry.
327 Among the SBF targets, G1 cyclins pose a major block to meiotic entry by interfering with
328 Ime1 function, critically at the level of Ime1-Ume6 interaction. While these findings
329 emphasize the importance of *SWI4* regulation to ensure timely SBF activity, the question
330 remains as to how SBF activity is downregulated during transition from mitosis to meiosis.
331

332 **Ime1-dependent expression of a LUTI from the *SWI4* locus leads to a reduction in**
333 **Swi4 protein levels during meiotic entry**

334 Given the importance of *SWI4* downregulation in restricting SBF activity during mitotic to
335 meiotic cell fate transition, we next investigated the mechanism of *SWI4* downregulation.
336 A previous study identified a long undecoded transcript isoform (LUTI) expressed from
337 the *SWI4* locus in meiotic cells (Brar et al., 2012, Figure 5A). When $SWI4^{LUTI}$ is expressed,
338 the canonical protein-coding *SWI4* transcript, $SWI4^{canon}$, is downregulated (Tresenrider et
339 al., 2021, Figure 5B), suggesting that LUTI expression restricts Swi4 protein levels and
340 thus SBF activity during meiotic entry.
341

342 To further investigate LUTI-based repression of *SWI4*, we examined the relationship
343 between $SWI4^{LUTI}$ and $SWI4^{canon}$ transcripts using single molecule RNA fluorescence in
344 situ hybridization (smFISH: Chen et al., 2017, 2018; Raj et al., 2008). Two distinct probes
345 were used: one, conjugated to Quasar 670 (Q670) and complementary to the *SWI4*
346 coding sequence (CDS) and the other, conjugated to CAL Fluor Red 590 (CF590) and
347 unique to the 5′ extended LUTI sequence. Accordingly, a spot where the two probe sets
348 colocalized indicated a $SWI4^{LUTI}$ transcript, whereas a spot marked with Q670 probe

349 alone highlighted a *SWI4*^{canon} transcript. We used a well-established meiotic cell
350 synchronization system (Berchowitz et al., 2013) to investigate the precise temporal
351 expression of these two mRNA isoforms. In comparison to premeiotic state, meiotic cells
352 displayed a significant increase in *SWI4*^{LUTI} transcripts ($p < 0.0001$, Mann-Whitney test)
353 as well as a significant decrease in *SWI4*^{canon} transcripts ($p = 0.0007$, Mann-Whitney test)
354 (Figure 5C and 5D), thus confirming their inverse expression pattern.
355
356 To characterize the functional contribution of the LUTI to *SWI4* downregulation, we
357 eliminated *SWI4*^{LUTI} production (Δ*LUTI*) by deleting its promoter (Tresenrider et al., 2021)
358 and used RNA blotting to visualize the *SWI4* mRNA isoforms. In wild-type cells, *SWI4*^{LUTI}
359 was readily detectable after 1 hour in SPO, corresponding to early meiotic entry (Figure
360 5E). During the time points when *SWI4*^{LUTI} was highly expressed, *SWI4*^{canon} transcript
361 levels were lower, consistent with the smFISH results revealing *SWI4*^{LUTI} and *SWI4*^{canon}
362 levels are anticorrelated. In Δ*LUTI* cells, we observed an increase in the abundance of
363 *SWI4*^{canon} mRNA (Figure 5E). This finding corroborates previous reports, where LUTI
364 expression leads to co-transcriptional silencing of the canonical gene promoter, thereby
365 silencing expression of the protein-coding transcript (Chen et al., 2017; Chia et al., 2017;
366 Van Dalfsen et al., 2018; Tresenrider et al., 2021; Vander Wende et al., 2022). Finally, by
367 immunoblotting, we observed an increase in Swi4 protein abundance in the Δ*LUTI* mutant
368 compared to wild type (Figure 5E and 5F), further indicating that *SWI4*^{LUTI} expression
369 downregulates Swi4 protein levels in meiosis.
370

371 *SWI4*^{LUTI} translation occurs within the upstream ORFs (uORFs) of its 5′ leader sequence
372 (Brar et al., 2012). If the uORFs repress productive translation of the *SWI4* CDS contained
373 within the LUTI, then their removal should result in increased Swi4 protein levels. To
374 determine whether the uORFs inhibit translation of the *SWI4* CDS, we mutated the start
375 codon of all seven uORFs within *SWI4*^{LUTI} from ATG to ATC (Δ*uORF*) and measured Swi4
376 protein levels using immunoblotting. Compared to wild type, the Δ*uORF* mutant had
377 higher levels of Swi4 protein (Figure 5G and 5H). RNA blotting confirmed that *SWI4*^{canon}
378 transcript levels remained similar between wild type and Δ*uORF* mutant, whereas
379 *SWI4*^{LUTI} levels were higher in the Δ*uORF* mutant compared to wild type (Figure 5G),
380 likely resulting from increased transcript stability due to bypass of nonsense mediated
381 decay (Tresenrider et al., 2021). Our findings indicate that the uORFs within the LUTI are
382 translated at the expense of *SWI4* CDS, thus halting Swi4 synthesis during early meiosis.
383
384 Our previous findings highlight an antagonistic relationship between Swi4 and Ime1
385 nuclear localization, whereby overexpression of *SWI4* leads to a decrease in Ime1
386 nuclear localization (Figure 2E). Given the previous finding that Ime1 activates
387 transcription of LUTIs in early meiosis (Tresenrider et al., 2021), we were curious whether
388 the reverse regulation could also occur, where Ime1 causes downregulation of Swi4
389 through activating *SWI4*^{LUTI} transcription. To test this possibility, we used an inducible
390 allele of *IME1* (*pCUP1-IME1*) (Chia and van Werven, 2016) and measured Swi4 protein
391 abundance. In the absence of *IME1* induction, Swi4 levels remained constant. However,
392 after 1 hour of *IME1* induction, Swi4 levels started to decrease dramatically (Figure 5I and
393 5J). Therefore, reduction in Swi4 levels is dependent on Ime1 rather than being driven by

394 nutrient deprivation in SPO, a condition that is known to trigger autophagy (Abeliovich
395 and Klionsky, 2001). To further assess whether *SWI4*^{LUTI} is regulated by the Ime-Ume6
396 transcription factor complex, we analyzed a published Ume6 ChIP-seq dataset
397 (Tresenrider et al., 2021) and found evidence for Ume6 binding at the *SWI4*^{LUTI} promoter
398 (Figure 5K). Additionally, analysis of an mRNA-seq dataset from *UME6-T99N*
399 (Tresenrider et al., 2021), an allele of *UME6* that can no longer interact with Ime1,
400 revealed a dramatic reduction in *SWI4*^{LUTI} expression in meiotic conditions (Figure S5).
401 Together, these data support the notion that Ime1-Ume6 complex induces the expression
402 of *SWI4*^{LUTI}, which in turn inhibits Swi4 protein synthesis through the combined act of
403 transcriptional and translational interference.
404

405 **_SWI4_^{LUTI} is integrated into a larger regulatory network to regulate SBF activity**
406 **during meiotic entry**

407 Since the removal of *SWI4*^{LUTI} resulted in an increase in Swi4 levels, we next wanted to
408 investigate how the loss of LUTI-based regulation affects meiotic entry. We performed
409 mRNA-seq in Δ*LUTI* mutant or wild-type cells during meiotic entry (2 h in SPO) and used
410 DESeq2 to identify differentially expressed genes. To our surprise, there was no obvious
411 increase in the expression of many SBF targets (Figure 6A). Namely, *CLN1* and *CLN2*
412 were both expressed at similar levels to wild type upon loss of *SWI4*^{LUTI}. Therefore, it
413 appears that disruption of the LUTI-based regulation alone is not sufficient to reactivate
414 SBF targets.
415

416 Since transition from the mitotic to meiotic program is a critical cell fate decision, it is likely
417 that additional players are in place to restrict SBF activity. In this case, even when the
418 LUTI-based regulation fails, SBF would remain largely inactive due to a backup
419 mechanism. In support of this notion and consistent with a previous report (Argüello-
420 Miranda et al., 2018), the SBF inhibitor Whi5 was expressed during early meiosis (0 h in
421 SPO) and localized to the nucleus (Figure S6A). During the mitotic G1 phase, Whi5
422 associates with promoter-bound SBF, thereby preventing the transcription of SBF target
423 genes (De Bruin et al., 2004; Costanzo et al., 2004). Shortly before the G1/S transition,
424 phosphorylation of Whi5 via the Cln3/CDK pathway activates SBF by promoting nuclear
425 export of Whi5 (De Bruin et al., 2004; Costanzo et al., 2004). However, in nutrient-
426 deprived conditions that favor meiosis such as nitrogen limitation, *CLN3* is translationally
427 repressed and any Cln3 protein that is expressed is also unstable (Parviz and Heideman,
428 1998; Gallego et al., 1997). Without Cln3/CDK, Whi5 is expected to inhibit SBF in a
429 constitutive manner.
430
431 To determine whether Whi5 and *SWI4*^{LUTI} act in parallel to restrict SBF activity, we
432 removed Whi5 from the nucleus using the anchor-away method, which enables
433 compartment-specific depletion of a target protein via inducible dimerization (Haruki et
434 al., 2008). Whi5 was tagged with FRB and ribosomal protein Rpl13a was tagged with
435 FKBP12. Upon addition of rapamycin, Rpl13a-FKBP12 and Whi5-FRB formed a
436 heterodimer, leading to successful nuclear exclusion of Whi5 (Figure 6B). Using Whi5
437 anchor away (*WHI5-AA)* alone or in combination with removal of LUTI-based *SWI4*
438 regulation (Δ*LUTI)*, we performed mRNA-seq to measure expression of SBF targets and

439 early meiotic genes. Similar to the Δ*LUTI* single mutant, *WHI5-AA* alone did not
440 significantly change the expression of SBF targets or early meiotic genes relative to wild
441 type (Figure 6C). However, loss of both modes of regulation resulted in increased
442 expression of SBF targets as well as a concomitant decrease in early meiotic transcripts
443 compared to wild type (Figure 6D, Supplemental Table 3). As expected, Swi4 levels were
444 similar to wild type in *WHI5-AA* but were elevated in Δ*LUTI* and Δ*LUTI*; *WHI5-AA* mutants
445 (Figure S6B). Gene set enrichment analysis revealed a significant enrichment of the SBF
446 regulon (NES = 1.95, $p < 0.001$) as well as significant disenrichment of the early meiotic
447 genes (NES = -3.39, $p < 0.001$) in the Δ*LUTI*; *WHI5-AA* double mutant (Figure S6C).
448
449 Finally, we monitored meiotic entry using time-lapse fluorescence microscopy in strains
450 carrying endogenously tagged Rec8-GFP in conjunction with Htb1-mCherry. In
451 agreement with our mRNA-seq data, loss of either LUTI- or Whi5-based repression of
452 SBF alone was not sufficient to cause a delay in meiotic entry (Figure 6E). However,
453 simultaneous perturbation of both pathways led to a significant delay in meiotic entry
454 (Figure 6E, $p = 0.0112$, Mann-Whitney test). These data further support the notion that
455 $SWI4^{LUTI}$ is integrated into a larger regulatory network to regulate SBF activity during
456 meiotic entry, which includes Whi5-mediated repression of SBF.
457
458 **DISCUSSION**
459 In this study we describe two distinct mechanisms by which meiotic cells inhibit the activity
460 of SBF, a transcription factor complex crucial for the G1/S transition during the mitotic cell
461 cycle. The dual inhibition of SBF converges on its unique subunit Swi4 and is important

462 for proper transition from mitotic to meiotic cell fate. Swi4 inhibition occurs through: (1)
463 meiosis-specific expression of a LUTI from the *SWI4* locus, *SWI4*^{LUTI}, which
464 downregulates Swi4 protein levels, and (2) repression of Swi4 activity by the Rb homolog
465 Whi5, which occurs even when the LUTI-based regulation is disrupted. Conditions that
466 lead to elevation of Swi4 levels at meiotic entry result in abrupt activation of the SBF and
467 a concomitant decline in the expression of early meiotic genes, leading to meiotic
468 progression delays. Additionally, we show that the SBF targets *CLN1* and *CLN2* are major
469 drivers of the meiotic entry defect resulting from SBF misregulation. The *CLN*-dependent
470 phenotypes can be largely rescued by tethering of the central meiotic regulator Ime1 to
471 its cofactor Ume6, suggesting that the primary reason for meiotic failure caused by these
472 G1 cyclins is due to a defect in Ime1-Ume6 interaction. Our findings reveal the functional
473 role of a LUTI in establishing the meiotic transcriptional program and demonstrate how
474 the LUTI-based regulation is integrated into a larger regulatory network to ensure timely
475 SBF activity, and provide mechanistic insights into how SBF misregulation impedes
476 transition from mitotic to meiotic cell fate (Figure 6F).
477

478 **Rewiring of the G1/S regulon**

479 It has long been known that entry into the mitotic cell cycle and meiotic differentiation are
480 regulated differently. During the mitotic cell cycle, budding yeast cells must reach a critical
481 size before commitment to division in late G1 phase, an event termed the “Start” (Hartwell
482 et al., 1974; Johnston et al., 1977). Start depends on the activation of the G1/S regulon
483 by SBF and MBF, which regulate ~200 genes that function in polarized growth,
484 macromolecular biosynthesis, DNA replication, and repair among other critical processes

485 (reviewed in Jorgensen and Tyers, 2004). In contrast, entry into meiosis requires the
486 transcriptional activator, Ime1, which is exclusively induced in diploid cells through the
487 integration of several extrinsic cues including nitrogen levels, carbon source and
488 extracellular pH (reviewed in van Werven and Amon, 2011). Ime1 initiates the first
489 transcriptional wave of early meiotic genes required for DNA replication, recombination,
490 and chromosome morphogenesis. Before our study, it was unclear whether and how
491 SBF-MBF activity is regulated during the transition from mitosis to meiosis, despite the
492 transcriptome-wide differences between these two developmental programs. We found
493 that during meiotic entry, the SBF-specific Swi4 subunit is downregulated, which indicates
494 that the activity of SBF, but not MBF, is constrained. Consistently, SBF-specific targets
495 display either low or no expression during early meiosis, while MBF targets are
496 upregulated upon meiotic entry. MBF targets are involved in processes shared between
497 mitosis and meiosis including DNA replication and repair, whereas SBF targets are
498 predominantly involved in processes unique to mitosis such as budding and cell wall
499 biosynthesis. This functional specialization might have enabled adaptations to
500 accommodate specific cell fates. Likewise, SBF-specific targets that are detrimental to
501 meiosis, such as the G1 cyclins (Colomina et al., 1999, and this study), might contribute
502 to the mutually exclusive nature of the mitotic and meiotic programs.
503
504 Absolute measurements of the concentrations of SBF and MBF in single cells during
505 mitotic G1 demonstrated that these transcription factors are sub-saturating with respect
506 to their target promoters in small cells, but that SBF and MBF levels increase as cells
507 grow, suggesting that their abundance is a limiting factor in activating the G1/S regulon

508 (Dorsey et al., 2018). Corroborating these findings, we show that overexpression of *SWI4*
509 as well as the simultaneous disruption of the two pathways that normally restrict SBF
510 activity at meiotic entry – namely LUTI and Whi5 – result in abrupt activation of the SBF
511 regulon and a concomitant decrease in early meiotic gene expression. However, MBF
512 targets do not seem to be affected in response to increased SBF activity. This is surprising
513 given that SBF and MBF share a common subunit, Swi6, and that an upsurge in Swi4
514 abundance might be expected to titrate Swi6 away from MBF. It is possible that meiosis-
515 specific regulators like Ime1 and Ime2 compensate to maintain MBF target expression
516 (Brush et al., 2012). Future studies are necessary to dissect the meiotic roles of MBF and
517 potential compensatory mechanisms.
518
519 **Inhibition of G1 cyclins during meiotic entry and vice versa**
520 We found that the meiotic entry delay due to untimely SBF activation can be partially
521 rescued by loss of either *CLN1* or *CLN2*, demonstrating that both cyclins are responsible
522 for the meiotic defects associated with SBF misregulation. In addition to *CLN1* and *CLN2*,
523 improper activation of SBF also leads to upregulation of *PCL1* during meiotic entry (Figure
524 2F and 6B). *PCL1* encodes a cyclin that interacts with the Pho85 CDK and is involved in
525 the regulation of polarized cell growth and morphogenesis as well as progression through
526 the cell cycle (Espinoza et al., 2016). Whether *PCL1* misexpression contributes to the
527 SBF-associated meiotic entry defects is an interesting avenue for future studies.
528
529 We and others have demonstrated that elevated levels of G1 cyclins inhibit meiotic entry.
530 Therefore, it is crucial to dissect the mechanisms that govern the downregulation of G1

531 cyclins during this process. Among the G1 cyclins that are known to inhibit meiotic entry
532 (Colomina et al., 1999), only the mechanism of *CLN3* restriction was previously known
533 (Parviz and Heideman, 1998; Gallego et al., 1997). Our study provides a mechanistic
534 understanding of how *CLN1* and *CLN2* remain quiescent during meiotic entry through the
535 combined act of LUTI-based and Whi5-dependent inhibition of SBF. Whether additional
536 mechanisms play a role in restricting SBF and/or *CLN1*-*CLN2* remains to be determined.
537
538 Our findings also shed light on the mechanism by which G1 cyclins prevent meiotic entry.
539 Previous work demonstrated that G1 cyclin overexpression leads to downregulation of
540 *IME1* expression and inhibition of Ime1 nuclear localization (Colomina et al., 1999). Even
541 though we observed similar defects in *IME1* in response to *CLN2* overexpression,
542 increasing *IME1* expression or targeting Ime1 to the nucleus did not result in successful
543 meiosis (Figure 4). Instead, we found that restoring the interaction between Ime1 and its
544 cofactor Ume6 was sufficient to bypass the meiotic blockage exerted by Cln/CDK.
545 Collectively, our analyses suggest that the primary reason why G1 cyclins cause a meiotic
546 failure is due to a deficiency in Ime1-Ume6 interaction.
547
548 Future work could be aimed at dissecting how G1 cyclins affect the interaction between
549 Ime1 and Ume6 and whether their impact on Ime1's subcellular localization is primarily
550 due to G1 cyclin-dependent changes in Ime1-Ume6 interaction. Since there are no CDK
551 consensus phosphorylation sites on Ime1 itself, other players are likely to be involved.
552 Rim11 and Rim15 are potential candidates since these two kinases have been implicated
553 in Ime1-Ume6 phosphorylation as well as regulation of Ime1 localization and its

554 interaction with Ume6 (Rubin-Bejerano et al., 1996; Vidan and Mitchell, 1997; Bowdish et
555 al., 1994). Interestingly, Rim15 contains CDK consensus phosphorylation sites (Holt et
556 al., 2009; Moreno-Torres et al., 2017; Breitkreutz et al., 2010), Furthermore, Cln2/CDK
557 activity has been previously shown to inhibit Rim15 nuclear localization (Talarek et al.,
558 2010), thereby making it an attractive candidate for further investigation.
559

560 **Antagonistic relationship between two key transcription factors, Swi4 and Ime1**

561 Swi4 and Ime1 regulate each other in an antagonistic manner (Figure 6F), as supported
562 by several observations. First, overexpression of *SWI4* leads to a reduction in Ime1
563 nuclear localization (Figure 2B). Second, premature activation of SBF through *SWI4*
564 overexpression or simultaneous disruption of *SWI4*^{LUTI} and Whi5 pathways results in a
565 significant delay in the chromosomal localization of Rec8, a direct transcriptional target of
566 Ime1 (Figure 2H, 2I and 6E). Additionally, many early meiotic genes that are also
567 transcriptional targets of Ime1 are downregulated under the same conditions (Figure 2F
568 and 6D). Third, *IME1* is inhibited by the G1 cyclins, which are themselves targets of
569 Swi4/SBF (Figure 4). The reverse regulation, where Ime1 inhibits Swi4, is also in place.
570 This occurs through the Ime1-dependent expression of *SWI4* ^{LUTI}, which is necessary to
571 downregulate Swi4 levels (Figure 5, also reported in Tresenrider et al., 2021). The
572 antagonistic relationship between Swi4 and Ime1 is further evidenced by their mutually
573 exclusive pattern of nuclear localization at the single-cell level (Figure 2E). In summary,
574 our study highlights the multiple ways in which Swi4 and Ime1 regulate each other, which
575 likely plays a crucial role in cellular decision making between the mitotic and meiotic
576 transcriptional programs.

577

578 **Intersection of LUTI-based gene repression with other regulatory pathways**

579 While LUTI-based regulation is both necessary and sufficient to downregulate Swi4
580 levels, disrupting it alone is not enough to activate the SBF regulon. We found that the
581 LUTI-based mechanism works together with the Whi5 pathway to inhibit SBF activity
582 (Figure 6). As a result, only when both mechanisms are simultaneously disrupted, do cells
583 exhibit abrupt activation of SBF targets and subsequent meiotic entry defects. This two-
584 pronged inhibition of SBF activity is reminiscent of how meiotic cells prevent microtubule-
585 kinetochore interactions during prophase I (Miller et al., 2012). Specifically, LUTI-based
586 regulation represses the expression of a limiting outer kinetochore subunit, Ndc80 (Chen
587 et al., 2017). Even when the outer kinetochore assembles upon disruption of *NDC80*^{LUTI},
588 microtubules are still unable to engage with the kinetochores due to restriction of Clb/CDK
589 activity. The loss of both regulations results in meiotic chromosome segregation defects
590 (Chen et al., 2017). Integrating LUTI-based repression into larger regulatory networks
591 likely ensures robustness in cellular decision-making, providing a fail-safe system.
592 However, combinatorial use of the LUTI-based mechanism with other regulatory
593 pathways poses a challenge to uncover their functional importance. Despite 8% of the
594 yeast genes being subject to LUTI-based regulation during meiosis (Cheng et al., 2018),
595 the biological significance of only two LUTIs, *NDC80*^{LUTI} and *SWI4*^{LUTI}, have been
596 uncovered thus far. Therefore, systematic studies aiming to dissect the biological roles of
597 LUTIs in meiosis and beyond would benefit from simultaneous perturbation approaches,
598 including synthetic genetic interactions.

599

600 **Concluding remarks**

601 Cell state changes are primarily governed by transcription factors. Our study highlights
602 how transition from mitotic to meiotic cell fate is ensured by inhibition of the SBF
603 transcription factor through two distinct mechanisms. The SBF regulon includes G1
604 cyclins, whose untimely expression blocks meiotic entry by interfering with Ime1, a master
605 transcriptional regulator of meiosis. SBF and Ime1 antagonize each other, thereby helping
606 establish a mutually exclusive state between the mitotic and meiotic transcriptional
607 programs.

608

609 Divergence of the G1/S transcription factors has been observed in mammalian cells.
610 Functional homologs of SBF and MBF in mammalian cells are known as E2Fs, nine of
611 which control the G1/S transition (reviewed in Van Den Heuvel and Dyson, 2008). Each
612 E2F regulates a distinct sets of genes (Gaubatz et al., 2000). Furthermore, some
613 members of the E2F family are involved in tissue-specific regulation of cell fate (Julian et
614 al., 2016). However, the molecular mechanisms driving the rewiring of these complex
615 gene networks are not well understood. Given the conservation of LUTI-based gene
616 regulation and Whi5 in mammalian cells (Hollerer et al., 2019; Hasan et al., 2014), our
617 studies may shed light into cell type specific regulations of Rb and E2Fs.

618
619

620 **MATERIALS AND METHODS**

621

622 **Strain Construction and Cloning**

623 All strains used in this study were derived from the SK1 background. Detailed information
624 about the strain genotypes can be found in Supplemental Table 4.

625

626 For *SWI4* (pUB1587) 1200 bases upstream of the ORF, *SWI4* ORF, C-terminal 3V5
627 epitope tag, and *SWI4* 3'UTR (1000 bases downstream of ORF) were cloned into a *LEU2*
628 single integration vector by Gibson assembly (NEB) (Gibson et al., 2009). LUTI promoter
629 deletion (Δ*LUTI*) strain (pUB1588) was similarly constructed with -1200 to -934 bases
630 upstream from ORF deleted. For the uORF mutant (Δ*uORF*) strain (pUB1734) all seven
631 ATG uORFs were mutated using gBlocks with the ATG>ATC mutations and cloned by
632 Gibson assembly into 3V5-tagged *LEU2* single integration vector. In all strains described
633 above, the endogenous *SWI4* gene is deleted using Pringle-based insertion of KanMX6
634 marker (Bähler et al., 1998).

635

636 For overexpression of *SWI4 (pUB1585)*, *CLN1 (pUB2144)*, and *CLN2 (pUB1899)*, the
637 relevant gene carrying a 3V5 epitope tag was cloned downstream of the *ATG8* promoter,
638 which is highly expressed during meiosis (Brar et al., 2012). A *LEU2* single integration
639 vector was used for cloning the fragments by Gibson assembly (*NEB*). In the strains
640 carrying overexpression transgenes, the wild-type alleles at the endogenous loci
641 remained intact. *pCUP1-GFP-IME1* allele was made with Pringle-based insertion of the
642 *pCUP1* promoter upstream of *GFP-IME1*. *PUS1*-αGFP and *UME6*-αGFP were made by
643 Pringle-based insertion using a plasmid (pUB1707) gifted by the Lackner Lab. For *WHI5-*
644 *AA* the *WHI5-mCherry-FRB* allele was made by Pringle-based insertion using a plasmid
645 (pUB595) gifted by the Nasmyth lab. All plasmid sequences were confirmed by
646 sequencing.

647

648 All single integration plasmids were digested with Pme1 before transformation. Proper
649 integration was confirmed by PCR. The plasmids constructed in this study are listed in
650 Supplemental Table 5.

651

652 **Sporulation Conditions**

653 For meiotic experiments using *pCUP1-IME1/pCUP1-IME4* or *pCUP-IME1* system, cells
654 were synchronized as described in (Chia and van Werven, 2016). Briefly, after 24 h of
655 growth in YPD at room temperature, saturated cultures (OD_{600} > 10) were diluted to an

656 OD_{600} of 0.25 in BYTA (1% yeast extract, 2% bacto tryptone, 1% potassium acetate, and
657 1.02% potassium phthalate) for 16-18 h of growth at 30°C (OD_{600} of > 5). Cells were
658 washed with water twice before final resuspension in SPO with 0.5% potassium acetate
659 to an OD_{600} of 1.85. After 2 h in SPO, *IME1* and *IME4* were induced with 50 μM $CuSO_4$.
660 Sporulation efficiency was measured after 24 h in SPO. Anchor away meiotic experiments
661 was performed as described above with final 1 μM rapamycin (Millipore) added to BYTA
662 30 minutes before transfer to SPO and again 1 μM rapamycin added to SPO media.
663
664 In all other meiotic experiments, cells were prepared as in (Carlile and Amon, 2008).
665 Briefly, after 24 h of growth in YPD at room temperature, saturated cultures (OD_{600} > 10)
666 were diluted to an OD_{600} of 0.25 and inoculated in BYTA (1% yeast extract, 2% bacto
667 tryptone, 1% potassium acetate, and 1.02% potassium phthalate) for 16-18 h at 30°C
668 (OD_{600} of > 5). Cells were washed with water twice before final resuspension in SPO with
669 0.5% potassium acetate to an OD_{600} of 1.85. Sporulation efficiency was counted after 24
670 h in SPO.
671
672 *UME6-αGFP* meiotic experiments were prepared as in (Chia and van Werven, 2016).
673 Briefly, after 18 h of growth in YPD at room temperature, saturated cultures (OD_{600} > 10)
674 were diluted to an OD_{600} of 0.2 in reduced YPD (1% yeast extract, 2% peptone, 2%
675 dextrose, uracil [24 mg/L]). Reduced YPD was used instead of BYTA to prevent cells from
676 prematurely entering meiosis in BYTA due to the Ime1-Ume6 interaction from the GFP
677 nanobody. Cells were grown for ~6 h at 30°C until they reached an OD_{600} between 0.5
678 and 1.0. Cultures were then back diluted to OD_{600} of 0.1 and grown for 18 h at 30°C. Cells
679 were washed with water twice before final resuspension in SPO with 0.5% potassium
680 acetate to an OD_{600} of 1.85. Sporulation efficiency was counted after 24 h in SPO.
681
682 **RNA Extraction for mRNA-seq, RT-qPCR, and RNA Blotting**
683 RNA extraction was performed as described in (Tresenrider et al., 2021). Briefly, ~4
684 OD unit of cells were pelleted by centrifugation for 1 minute at 20,000 rcf and snap frozen
685 in liquid nitrogen. Cells were thawed on ice and resuspended in TES buffer (10 mM Tris
686 pH 7.5, 10 mM EDTA, 0.5% SDS). An equal volume of Acid Phenol:Chloroform:Isoamyl

687 alcohol (125:24:1; pH 4.7) was added to cells and incubated at 65°C for 45 min shaking
688 at 1400 rpm. Aqueous phase was transferred to a new tube with chloroform, vortexed for
689 30 sec, separated by centrifugation, and precipitated in isopropanol and sodium acetate
690 overnight at -20°C. Pellets were washed with 80% ethanol and resuspended in DEPC
691 water for 10 min at 37°C. Total RNA was quantified using a nanodrop.
692
693 **mRNA Sequencing (mRNA-seq) and Analysis**
694 RNA-seq libraries were generated with the NEXTflex™ Rapid Directional mRNA-Seq Kit
695 (NOVA-5138, Perkin Elmer). 10 µg of total RNA was used as input for all
696 libraries. AMPure XP beads (A63881, Beckman Coulter) were used to select fragments
697 between 200-500 bp. Libraries were quantified using the Agilent
698 4200 TapeStation (Agilent Technologies, Inc). Samples were submitted for 100 bp SE
699 sequencing by the Vincent J. Coates Genomics Sequencing Laboratory with a NovaSeq
700 SP 100SR.
701
702 Hisat2 (Kim et al., 2019) was used to align reads to map sequences to SK1 PacBio
703 genome. Quantification of RNA as transcripts per million was done StringTie (Pertea et
704 al., 2015). Fold-change quantification was performed by DESeq2 using default options
705 (version 1.34.0, (Love et al., 2014)).
706
707 For Gene Set Enrichment Analysis (GSEA) v4.3.2 was used to compare TPM values for
708 different gene sets. The early meiotic gene set was created from Figure 2 of (Brar et al.,
709 2012). The SBF regulon was from Figure 3 of (Iyer et al., 2001). GSEA was performed
710 on the desktop app with default settings expect “Collapse/Remap to gene symbols” was
711 set to “No_Collapse” and “Permutation type" was set to "gene_set”.
712
713 For Gene Ontology (GO) Analysis, SGD Gene Ontology Slim Term Mapper was used for
714 GO analysis using Yeast Go-Slim: process GO Set. Used output from DE-Seq2 analysis
715 with a cutoff of padj (P value) < 0.05.
716

717 The two overlapping targets (*SWE1* and *TOS4*) between the early meiotic gene set and
718 SBF targets are not plotted on volcano plot or used for GSEA analysis.
719
720 **Reverse Transcription-Quantitative Polymerase Chain Reaction (RT-qPCR)**
721 5 μg of isolated total RNA was treated with DNase (TURBO DNA-free^{TM} Kit). cDNA was
722 reverse transcribed following the Superscript III kit (ThermoFisher Scientific).
723 Quantification was performed with Absolute Blue qPCR Mix (ThermoFisher Scientific).
724 Meiotic samples were normalized to *PFY1,* and mitotic samples were normalized to
725 *ACT1.* Oligonucleotides are listed in Supplemental Table 6.
726
727 **Protein Extraction and Immunoblotting**
728 ~4 OD_{600} of cells were collected and pelleted by centrifugation for 1 min at 20,000 rcf.
729 Pellet was resuspended in 5% (w/v) TCA for at least 15 min at 4°C. Cells were washed
730 with TE50 (50 mM Tris-HCl [pH 7.5], 1 mM EDTA) and then with 100% acetone. The cell
731 pellet was dried overnight and then lysed with glass beads in lysis buffer (Tris-HCl [pH
732 7.5], 1 mM EDTA, 2.75 mM DTT, protease inhibitor cocktail (cOmplete EDTA-free
733 [Roche]). Next 3x SDS sample buffer (187.5 mM Tris [pH 6.8], 6% β-mercaptoethanol,
734 30% glycerol, 9% SDS, 0.05% bromophenol blue) was added and the cell lysate was
735 boiled for 5 min at 95°C. Protein was separated by PAGE using 4-12% Bis-Tris Bolt gels
736 (Thermo Fisher) and transferred onto 0.45 µm nitrocellulose membranes.
737
738 Cln1-3V5, Cln2-3V5 and GFP-GFP tagged proteins were all transferred onto 0.45 µm
739 nitrocellulose membranes using a semi-dry transfer apparatus (Trans-Blot Turbo System
740 (Bio-rad)). Swi4-3V5 or untagged Swi4, Swi6, and Mbp1 proteins were all transferred onto
741 0.45 µm nitrocellulose membranes using a PROTEAN Tetra tank (BioRAD) filled with 25
742 mM Tris, 192 mM glycine, and 7.5% methanol. All blots were incubated at room
743 temperature with Odyssey Blocking Buffer (PBS) (LI-COR Biosciences).
744
745 Immunoblotting for Cln1-3V5, Cln2-3V5, and GFP-Ime1 was performed as previously
746 described in (Tresenrider et al., 2021). Briefly, mouse α-V5 antibody (R960-25, Thermo
747 Fisher) or mouse α-GFP antibody (632381, Takara) were diluted 1:2000 in Odyssey

748 Blocking Buffer (PBS) (LI-COR Biosciences) with 0.01% Tween. Rabbit α-hexokinase (α-
749 Hxk2) antibody (H2035, US Biological) was diluted to 1:20,000. Secondary antibodies
750 used were α-mouse antibody conjugated to IRDye 800CW (926-32212, LI-COR
751 Biosciences) and α-rabbit antibody conjugated to IRDye 680RD (926-68071, LI-COR
752 Biosciences). Secondary antibodies were diluted to 1:20,000 in Odyssey Blocking Buffer
753 (PBS) with 0.01% Tween.
754
755 For immunoblotting of Swi4, Swi6, and Mbp1. antibodies specific to each subunit were a
756 generous gift from the Andrews and deBruin labs (Andrews and Herskowitz, 1989; Harris
757 et al., 2013). α-Swi4, α-Swi6, α-Mbp1 antibodies were each diluted to 1:2000 in Odyssey
758 Blocking Buffer (PBS) (LI-COR Biosciences) with 0.01% Tween. Secondary antibodies
759 included a α-rabbit antibody conjugated to IRDye 800CW (926-32213, LI-COR
760 Biosciences) and a α-rabbit antibody conjugated to IRDye 680RD (926-68071, LI-COR
761 Biosciences).
762
763 Odyssey system (LI-COR Biosciences) was used to image the blots, and Image Studio
764 Lite (LI-COR Biosciences) was used for image quantification.
765
766 **Northern (RNA) Blotting**
767 For each blot, 10 µg of total RNA was dried in a Savant Speed Vac (SPD111V). RNA was
768 then resuspended and denatured in glyoxal/DMSO mix (1M deionized glyoxal, 50% v/v
769 DMSO, 10 mM sodium phosphate (NaPi) buffer [pH 6.8]) at 70°C for 10 min. RNA sample
770 was loaded into an agarose gel (1.1% [w/v] agarose in 0.01 M NaPi buffer) with loading
771 dye (10% v/v glycerol, 2 mM NaPi buffer [pH 6.8], ~0.25% w/v xylene cyanol, and orange
772 G) and ran for 3 h at 100 V with a Variable Speed Pump (BioRad) to circulate buffer during
773 the entire gel run.
774
775 RNA was transferred overnight to nylon membrane (Hybond-N+ [GE]) in SSC. Membrane
776 was crosslinked using a Stratalinker UV Crosslinker (Stratagene). Ribosomal RNA
777 (rRNA) bands were visualized with methylene blue staining and imaged on a Gel Doc
778 XR+ Molecular Imager with Image Lab software (BioRad).

779

780 Probe templates containing the T7 promoter were amplified using PCR. PCR product was
781 concentrated with MinElute Spin Columns (Qiagen) and then used for *in vitro* transcription
782 to generate a strand-specific RNA probe using a MaxiScript T7 Kit (Invitrogen) according
783 to the manufacturer's instructions, except cold UTP was replaced with α-P32 labeled UTP
784 (PerkinElmer). Excess nucleotides were removed with NucAway Spin Columns
785 (Invitrogen). Blots were blocked in ULTRAhyb Ultrasensitive Hybridization Buffer
786 (Invitrogen) for 1 h and then incubated with the α-P32 labeled probe overnight at 68°C.
787 Blots were then washed twice with low stringency wash buffer (2X SSC, 0.1% SDS) for
788 10 min and then washed twice with high stringency wash buffer (0.1X SSC, 0.1% SDS)
789 for 15 min. Blots were then exposed overnight on a storage phosphor screen (Molecular
790 Dynamics) and then imaged on a Typhoon phosphor-imaging system.

791

792 **Fluorescence Microscopy**

793 For time course imaging of cells expressing *GFP-IME1*, *SWI4-mCherry*, or *WHI5-*
794 *mCherry*, 500 µL of meiotic culture was fixed with a final concentration of 3.7%
795 formaldehyde (v/v) at room temperature for 15 min. Cells were then washed in 1 ml of
796 100 mM potassium phosphate [pH 6.4] and stored at 4°C in 20 µl of KPi Sorbitol solution
797 overnight (100 mM potassium phosphate [pH 7.5], 1.2M sorbitol). Cells were mounted on
798 a slide and imaged using DeltaVision Elite wide-field fluorescence microscope (GE
799 Healthcare) with a 60x/1.516 oil immersion objective. Deconvolution of images was done
800 with softWoRx imaging software (GE Life Sciences).

801

802 For live-cell imaging, cells at OD_{600} of 1.85 in conditioned SPO (filter-sterilized SPO
803 culture after ~5 h in 30°C) were sonicated and transferred to a concanavalin A (Sigma)
804 treated 96-well clear, flat bottom plate (Corning). Four z positions (2 µm step size) were
805 acquired per XY position. Acquisition was performed in a temperature-controlled chamber
806 at 30°C. Please refer to Supplemental Table 7 for acquisition settings.

807

808 **Image Quantification**

809 All image analysis was performed with FIJI (Schindelin et al., 2012). Maximum z-
810 projection are shown in figures and were modified using linear brightness and contrast
811 adjustments in FIJI.
812
813 To quantify localization of GFP-Ime1 and Rec8-GFP, z-slices containing the nucleus were
814 selected using the Htb1-mCherry signal. Max projection was created from these slices
815 and GFP-Ime1 was scored double-blinded as nuclear or not nuclear.
816
817 For mean nuclear intensity of GFP-Ime1 and Swi4-mCherry, an individual z-slice
818 containing the nucleus was selected and nuclear mask was generated using the Htb1-
819 mCherry signal. The nuclear mask was then used to quantify the mean nuclear intensity
820 of GFP-Ime1 signal.
821
822 **Single molecule RNA FISH**
823 smFISH was performed and quantified as previously described in (Chen et al., 2018). All
824 probes were ordered from (Biosearch Technologies). Unique region of *SWI4*^{LUTI} was
825 visualized by twenty-eight 20-mer oligonucleotide probes coupled to CAL fluor Red 590.
826 Thirty-eight 20-mer probes coupled to Quasar 670 dye targeted to *SWI4*^{canon}. ~ 4 OD unit
827 of cells were fixed in final 3% formaldehyde (v/v) and incubated at room temperature for
828 20 minutes. Fixed samples were moved to 4°C to continue fixing overnight. Cells were
829 washed three times in cold Buffer B (0.1 M potassium phosphate [pH 7.5], 1.2 M sorbitol)
830 and resuspended in digestion buffer (Buffer B, 200 mM Vanadyl ribonucleoside complex
831 [VRC from NEB], zymolyse [zymolase 100T, MP Biomedicals]). Cells were digested at
832 30°C for 20 min and then gently washed with 1 mL of cold Buffer B and resuspended in
833 1 mL of 70% ethanol for 3.5-5 h.
834
835 Cells were then incubated in 1mL of 10% formamide wash buffer (10% formamide, 2X
836 SSC) at room temperature for 15 minutes. For hybridization, each probe set was added
837 (final concentration of 500 nM) to 20mM VRC and hybridization buffer (1% Dextran sulfate
838 [EMD Millipore], 1 mg/mL E. coli tRNA [Sigma], 2 mM VRC, 0.2 mg/mL BSA, 1X SSC,
839 10% formamide in nuclease-free water). Hybridization was done overnight at 30°C.

840 Samples were incubated in the dark for 30 min at 30°C in 1 mL of 10% formamide wash
841 buffer. Buffer was then removed, and cells were stained with DAPI and resuspended in
842 glucose-oxygen-scavenging buffer or GLOX buffer (10 mM Tris [pH 8.0], 2x SSC, 0.4%
843 glucose) without enzymes. Before imaging, GLOX solution with enzyme (1% v/v catalase,
844 1% v/v glucose oxidase (Sigma), 2 mM Trolox (Sigma)) was added to sample.
845
846 Images were acquired with the DeltaVision microscope as described in previous section
847 with filters: TRITC (EX542/27, EM597/45) for CAL Fluor Red 590 and CY5 (EX632/22,
848 EM679/34) for Quasar 670. Series of z-stacks (15–25 slices) were acquired with a step
849 size of 0.2 μm.
850
851 Matlab script (Chen et al., 2017, 2018) was run to quantify FISH spots with max intensity
852 projection of z-stacks. The same "signal" and "SNR" thresholds were applied to all the
853 images within a replicate.
854
855 **Resource availability**
856 All reagents used in this study are available upon request from the corresponding author.
857 Sequencing data generated in this study are available at NCBI GEO under the accession
858 ID: GSE225963
859 The custom code used for the analysis is available in the following code repository:
860 https://github.com/elifesciences-publications/Chen_Tresenrider_et_al_2017
861 **Acknowledgements:**
862 We thank Gloria Brar, Nick Ingolia, Rebecca Heald, Jingxun Chen, Anthony Harris,
863 Andrea Higdon, Grant King, Jessica Leslie, Kate Morse, Emily Powers Cyrus Ruediger,
864 Tina Sing, and Ben Styler for suggestions and comments on this manuscript, David
865 McSwiggen and Yuichiro Iwamoto for technical support, all members of the Ünal and Brar
866 labs and Jeremy Thorner for valuable discussions. This work is supported by funds from

867 the National Institutes of Health (R01 GM140005) and Astera Institute to E.Ü. and a
868 National Institutes of Health Traineeship (T32 GM007232) to A.J.S.

869 **Author contributions:**

870 A.J.S, conceptualization, data curation, formal analysis, investigation, methodology,
871 validation, visualization, and drafting of the manuscript. S.C.Y, data curation, formal
872 analysis, investigation, methodology, validation, visualization. E.Ü., conceptualization,
873 methodology, visualization, supervision, project administration, funding acquisition, and
874 drafting of the manuscript.

875

876 **Figure Legends**

877

878 **Figure 1. Swi4 subunit of the SBF and SBF targets are downregulated during early**
879 **meiosis**

880 **A.** A schematic of SBF and MBF complexes and the general functional groups of the
881 genes they regulate. **B.** Samples from strain UB35246 were collected between 0-6 hours
882 (h) in sporulation medium (SPO) and immunoblots were performed using α-Swi4, α-Swi6,
883 and α-Mbp1 respectively. Hxk2 was used a loading control. Representative blots from
884 one of two biological replicates are shown. **C.** Quantification of the immunoblots in (B).
885 The signal at each time point was first normalized to Hxk2 loading control and then to the
886 max signal. **D.** Scatterplot of RNA-seq data (RPKM) from (Brar et al., 2012) comparing 2
887 h in SPO vs. mitotic growth of well characterized SBF targets (pink) and MBF targets
888 (teal). **E.** Wild type (UB22199) and *pATG8-SWI4* (UB22226) cells were collected to
889 perform RT-qPCR for *CLN1, CLN2, CDC21,* and *RNR1* transcripts. Transcript abundance
890 was quantified using primer sets specific for each respective gene from three technical
891 replicates for each biological replicate. Quantification was performed in reference to *PFY1*

892 and then normalized to wild-type control. FC = fold change. Experiments were performed
893 twice using biological replicates, mean value plotted with range. Differences in wild type
894 versus *pATG8-SWI4* transcript levels at 2 h in SPO compared with a two-tailed t-test (*,
895 p = 0.0351 [*CLN1*]; **, p = 0.0013 [*CLN2*]; ns, p = 0.8488 [*CDC21*]; ns, p = 0.0859
896 [*RNR1*]). **F.** Live-cell imaging of strains containing the fluorescently tagged histone Htb1-
897 mCherry for wild type (UB32085) and *pATG8-SWI4* (UB32089). Experiments were
898 performed twice using biological replicates, mean value plotted with range. Differences in
899 meiotic progression tested by Mann Whitney test, two-tailed (**, p = 0.0045).
900

901 **Figure 2. Regulation of Swi4 abundance is required for timely meiotic entry**

902 **A-B.** Fixed imaging of cells marked with GFP-Ime1 and Htb1-mCherry. Wild type
903 (UB22199) and *pATG8-SWI4* (UB22226) cells were collected between 0-4 h in SPO. **A.**
904 Representative images with merge at 0 h and 2 h in SPO. Representative cells outlined.
905 Scale bar: 3 μm. **B.** Quantification as percent cells with nuclear Ime1. Experiments were
906 performed twice using biological replicates, mean value plotted with range. Total of 200
907 cells analyzed per strain. Differences in the fraction of cells with nuclear Ime1 was
908 compared using a two- tailed t-test (**, p = 0.0099 [1 h in SPO]; *, p = 0.0169 [2 h in SPO];
909 *, p = 0.0315 [3 h in SPO]; ns, two-tailed p = 0.4595 [4 h in SPO]). **C-E.** Fixed imaging of
910 cells marked with GFP-Ime1 and Swi4-mCherry. Wild type (UB31378) and *pATG8-SWI4*
911 (UB31381) cells were collected at 0 h and 4 h in SPO. **C.** Example images with merge at
912 4 h in SPO. Example cells outlined (*low nuclear GFP-Ime1 with high nuclear Swi4-
913 mCherry, **high nuclear GFP-Ime1 with low nuclear Swi4-mCherry). Scale bar: 3 μm. **D.**
914 Scatterplot of GFP-Ime1 mean nuclear intensity and Swi4-mCherry mean nuclear

915 intensity for wild type and *pATG8-SWI4* cells at 0 h in SPO. See Materials and Methods
916 for further details about image quantification. Dashed line is linear regression plotted for
917 each condition and strain. A total number of 269 cells were analyzed. **E.** Same as in (D)
918 but for wild type and. *pATG8-SWI4* cells at 4 h in SPO. A total number of 341 cells were
919 analyzed. Differences in mean nuclear GFP-Ime1 or Swi4-mCherry intensity between wild
920 type and *pATG8-SWI4* compared using a Mann-Whitney test, two-tailed (****, $p < 0.0001$
921 [wild type vs. *pATG8-SWI4* (GFP-Ime1)]; ****, $p < 0.0001$ [wild type vs. *pATG8-SWI4*
922 (Swi4-mCherry)]). **F.** Volcano plot of DE-Seq2 analysis for *pATG8-SWI4* versus wild type.
923 Dashed line indicates padj (p value) = 0.05. Analysis was performed using mRNA-seq
924 from two biological replicates. Wild type (UB22199) and *pATG8-SWI4* (UB22226) cells
925 were collected at 2 h in SPO. SBF targets (pink) (Iyer et al., 2001) and early meiotic genes
926 (blue) defined by (Brar et al., 2012). Darker pink or darker blue, labeled dots are well
927 studied targets in either gene set list. **G.** GSEA analysis of mRNA-seq comparing wild
928 type vs. *pATG8-SWI4* collected at 2 h in SPO. Vertical black bars represent the early
929 meiotic cluster from (Brar et al., 2012) or SBF cluster from (Iyer et al., 2001). The heatmap
930 indicates genes that are more enriched in *pATG8-SWI4* (red, left-side) or genes that are
931 enriched in wild type (blue, right-side). NES = normalized enrichment score. Enrichment
932 was determined by comparing *pATG8-SWI4* versus wild type. **H-I.** Live-cell imaging of
933 cells in meiosis marked by Rec8-GFP and nuclear marker Htb1-mCherry for wild type
934 (UB32085) and *pATG8-SWI4* (UB32089). **H.** Movie montage with example images
935 throughout meiosis for Rec8-GFP and Htb1-mCherry. Scale bar: 3 μm **I.** Quantification
936 as percent of cells that entered meiosis assayed by nuclear Rec8 appearance.
937 Experiments were performed using two biological replicates, mean value plotted with

938 range. A total number of 452 cells were analyzed. Differences in meiotic progression
939 compared by Mann Whitney test, two-tailed (***, p = 0.0005 [wild type vs. *pATG8-SWI4*]).
940

941 **Figure 3. Removal of the SBF targets Cln1 or Cln2 partially rescues the meiotic**
942 **entry delay in the *pATG8-SWI4* mutant**

943 **A.** Immunoblotting was performed on samples collected for wild type (UB29326) and
944 *pATG8-SWI4* (UB29328) between 0-6 h in SPO using α-V5 antibody to track Cln1-3V5.
945 Hxk2 was used a loading control. Representative blots from one of two biological
946 replicates are shown. **B.** Quantification of (A). **C.** Same as in (A) but for wild type
947 (UB29330) and *pATG8-SWI4* (UB29332) cells using α-V5 antibody to track Cln2-3V5.
948 Hxk2 was used a loading control. Representative blots from one of two biological
949 replicates are shown. **D.** Quantification of (C). **E.** Live-cell imaging of meiotic cells marked
950 by Rec8-GFP and nuclear marker Htb1-mCherry, with the following genotypes: wild type
951 (UB32085), *pATG8-SWI4* (UB32089), and *pATG8-SWI4*; *cln1*Δ (UB34536).
952 Quantification of cells that entered meiosis assayed by the initial timing of nuclear Rec8
953 appearance. Experiments were performed using two biological replicates, mean value
954 plotted with range. A total number of 883 cells were analyzed. Differences in meiotic
955 progression compared by Mann-Whitney test, two-tailed (*, p = 0.0111 [*pATG8-SWI4* vs.
956 *pATG8-SWI4*; *cln1*Δ]). *cln1*Δ alone (not shown) has similar meiotic progression kinetics
957 relative to wild type. **F.** Same as (E) but with the following genotypes: wild type
958 (UB32085), *pATG8-SWI4* (UB32089), and *pATG8-SWI4*; *cln2*Δ (UB34165). A total
959 number of 610 cells were analyzed. Differences in meiotic progression compared by

960 Mann-Whitney test, two-tailed (*, p = 0.0478 [*pATG8-SWI4* vs. *pATG8-SWI4*; *cln2*Δ]).
961 *cln2*Δ alone (not shown) has similar meiotic progression kinetics relative to wild type.
962
963 **Figure 4. Tethering of Ime1 to Ume6 is sufficient to overcome the meiotic block**
964 **exerted by G1 cyclin overexpression**

965 **A.** Sporulation efficiency of cells at 24 h in SPO media wild type (UB22199), *pATG8-*
966 *CLN1* (UB32820), *pATG8-CLN2* (UB25959), *pCUP-GFP-IME1* (UB34641), *pCUP1-GFP-*
967 *IME1; pATG8-CLN2* (UB35057), *PUS1-αGFP* (UB35593), *PUS1-αGFP; pATG8-CLN2*
968 (UB35982), *UME6-αGFP* (UB35300), and *UME6-αGFP; pATG8-CLN2* (UB35177).
969 Experiments shown in this figure were performed using two biological replicates, mean
970 value plotted with range. Total of 200 cells counted per strain. See Supplementary Table
971 2 for statistics. **B-C.** Fixed imaging of cells marked with GFP-Ime1 and Htb1-mCherry.
972 Wild type (UB22199) and *pATG8-CLN2* (UB25959) cells were collected between 0-3 h in
973 SPO. **B.** Representative images with merge at 2 h in SPO. Representative cells outlined.
974 Scale bar: 3 µm. **C.** Quantification of cells with nuclear Ime1. Experiments were performed
975 using two biological replicates, mean value plotted with range. Total of 200 cells analyzed
976 per strain. Differences in percent of cells with nuclear Ime1 was compared by two-tailed
977 t-test (**, p = 0.00917 [1 h in SPO]; **, p = 0.0044 [2 h in SPO]; *, p = 0.0122 [3 h in SPO]).
978 **D.** Schematic depicting use of *pCUP1* promoter (*pCUP1-GFP-IME1*) to rescue Ime1
979 transcript and protein levels. **E-F** Fixed imaging of cells marked with GFP-Ime1 and Htb1-
980 mCherry. Cells with the following genotypes were collected at 2 h in SPO: wild type
981 (UB22199), *pATG8-CLN2* (UB35106), *pCUP1-GFP-IME1* (UB34641), and *pCUP1-GFP-*
982 *IME1; pATG8-CLN2* (UB35057). **E.** Representative images with merge and

983 representative cells outlined. Scale bar: 3 μm. **F.** GFP-Ime1 mean nuclear intensity
984 measured for a single z-slice. A total number of 433 cells were analyzed. Differences in
985 mean nuclear intensity compared by Mann-Whitney test, two tailed, (****, $p < 0.0001$
986 [*pCUP1-IME1* vs. *pCUP1-IME1; pATG8-CLN2*]). **G.** Schematic of nanobody trap strategy
987 with *PUS1-αGFP* and GFP-Ime1 to rescue Ime1 nuclear localization in meiosis. **H-I.** Fixed
988 imaging of cells marked with GFP-Ime1 and Htb1-mCherry. Cells with the following
989 genotypes were collected at 2 h in SPO: wild type (UB22199), *pATG8-CLN2* (UB35106),
990 *PUS1-αGFP* (UB35593), and *PUS1-αGFP; pATG8-CLN2* (UB35982). **H.** Representative
991 images with merge and example cells outlined. Scale bar: 3 μm. **I.** GFP-Ime1 mean
992 nuclear intensity measured for a single z-slice. A total number of 934 cells were analyzed.
993 Differences in mean nuclear intensity compared by Mann-Whitney test, two-tailed, (****,
994 $p < 0.0001$ [wild type vs. *pATG8-CLN2*]; not significant (ns), $p = 0.6563$ [*PUS1-αGFP* vs.
995 *pATG8-CLN2; PUS1-αGFP*]; not significant (ns), $p = 0.8881$ [wildtype vs. *pATG8-CLN2;*
996 *PUS1-αGFP]*). **J.** Schematic of nanobody trap strategy with *UME6-αGFP* and GFP-Ime1
997 to rescue Ime1-Ume6 interaction in meiosis. **K-L** Fixed imaging of cells marked with GFP-
998 Ime1 and Htb1-mCherry. Cells with the following genotypes were collected at 2 h in SPO:
999 wild type (UB22199), *pATG8-SWI4* (UB35106), *UME6-αGFP* (UB35300), and *UME6-*
1000 *αGFP; pATG8-CLN2* (UB35177). **K.** Representative images with merge and
1001 representative cells outlined. Scale bar: 3 μm. **L.** GFP-Ime1 mean nuclear intensity
1002 measured for a single z-slice. A total number of 1220 cells were analyzed. Differences in
1003 mean nuclear intensity compared by Mann-Whitney test, two-tailed (****, $p < 0.0001$ [wild
1004 type vs. *pATG8-CLN2]*; ****, $p < 0.0001$ [*UME6-αGFP* vs. *pATG8-CLN2; UME6-αGFP*];
1005 *, $p = 0.0354$ [wildtype vs. *pATG8-CLN2; UME6-αGFP*]).

1006

1007 **Figure 5. Ime1-dependent expression of a LUTI from the *SWI4* locus leads to a**

1008 **reduction in Swi4 protein levels during meiotic entry**

1009 **A.** Genome browser views of RNA-seq data (Brar et al., 2012) of the *SWI4* locus. *SWI4*^{LUTI}

1010 transcription start site is ~1045bp upstream of *SWI4* ORF translation start site. **B.** A

1011 schematic of LUTI-based gene regulation. Top: Mitotic growth, *SWI4*^{LUTI} is repressed due

1012 to Ume6-Rpd3-Sin3 complex and *SWI4*^{canon} is induced by one or more transcription

1013 factors including Ace2, Mbp1 and Swi5, leading to Swi4 protein production. Bottom:

1014 Meiosis-specific expression of *SWI4*^{LUTI} by Ime1-Ume6 leads to downregulation of Swi4

1015 protein production due to combined effect of transcriptional and translation interference.

1016 *SWI4*^{LUTI} 5′ leader contains 7 AUG uORFs but only one is shown in the model for

1017 simplicity. Schematic is adapted from (Tresenrider et al., 2021). **C.** Representative

1018 smFISH images collected from premeiotic and meiotic cells for detecting *SWI4*^{canon} and

1019 *SWI4*^{LUTI}. Cells with *pCUP1-IME1/pCUP1-IME4* meiotic synchronization system were

1020 induced to enter meiosis with 50 μM $CuSO_4$ after 2 h in SPO. Premeiotic cells were

1021 collected before *IME1/4* induction and meiotic cells were collected 2 h post *IME1/4*

1022 induction from strain UB14273. Q 670 probes (green) hybridize to shared region within

1023 *SWI4* CDS. CF590 probes hybridize to the unique 5′ leader region of *SWI4*^{LUTI} (depicted

1024 on the schematic shown above the images). DNA was stained with DAPI. Scale bar: 3

1025 μm. **D.** Quantification of smFISH shown in (C), plotted as relative frequency histograms

1026 of cells with *SWI4*^{canon} and *SWI4*^{LUTI} transcripts per cell. Data pooled from two

1027 independent biological replicates. Dashed line indicates median number of transcripts per

1028 cell. Each histogram is normalized with maximum bin height being the same across all

1029 histograms. A total number of 44 cells counted for premeiotic and 102 cells counted in
1030 meiotic prophase. Differences in premeiotic versus meiotic were compared by Mann-
1031 Whitney test, two-tailed (***, p = 0.0007 [*SWI4*^{canon}]; ****, p < 0.0001 [*SWI4*^{LUTI}]). **E.** RNA
1032 blot performed on cells collected between 0-6 h in SPO. All strains carry a *SWI4-3V5*
1033 tagged allele. Probe was specific for 3V5. Methylene blue staining of rRNA bands was
1034 used as a loading control. Matched immunoblotting was performed against Swi4-3V5
1035 using α-V5 and normalized to Hxk2 loading control for each sample. Cells collected are
1036 wild type (UB22199) and Δ*LUTI* (UB23012). Representative blots from one of two
1037 biological replicates are shown. **F.** Quantification of immunoblot in (E). **G.** Performed as
1038 described in (E) for wild type (UB21386) and Δ*uORF* (UB23636) strains. Representative
1039 blots from one of two biological replicates are shown. **H.** Quantification of immunoblot in
1040 (G). **I.** Immunoblot using α-V5 performed on cells collected between 0-7 h in SPO from a
1041 strain carrying *pCUP1-IME1* and *SWI4-3V5* alleles (UB34641). Swi4-3V5 abundance was
1042 normalized to Hxk2 loading control. Cells were induced to enter meiosis with 50 μM
1043 $CuSO_4$ after 2 h preincubation in SPO. Representative blots from one of two biological
1044 replicates are shown. **J.** Quantification of immunoblot in (I). **K.** Genome browser view of
1045 Ume6-ChIP at the *SWI4* locus (adapted from Tresenrider et al., 2021).
1046

1047 **Figure 6. *SWI4*^{LUTI} is integrated into a larger regulatory network to regulate SBF**
1048 **activity during meiotic entry**

1049 **A.** Volcano plot of DESeq2 analysis for Δ*LUTI* versus wild type. Dashed line indicates
1050 padj (p-value) = 0.05. Analysis was performed with mRNA-seq in duplicate. Wild type
1051 (UB27083) and Δ*LUTI* (UB26874) collected at 2 h in SPO. SBF targets (pink) and early

1052 meiotic genes (blue) defined by (Iyer et al., 2001 and; Brar et al., 2012). Darker pink or
1053 darker blue, labeled dots are well studied targets in either gene set list. **B.** Top: Schematic
1054 of the anchor-away system using *WHI5-mCherry-FRB* (*WHI5-AA*) and *RPL13a-FKBP12*
1055 alleles. Bottom: Fixed imaging of cells marked with *WHI5-mCherry-FRB* (*WHI5-AA*) with
1056 DNA stained with DAPI. 1 μM rapamycin added at 0 h in SPO to induce nuclear exclusion
1057 of Whi5 (UB25431) strain collected at 0.5 h in SPO. Scale bar: 3 μm. Cells are rapamycin
1058 resistant due to mutated *TOR1* (*tor1-1*) and frp1Δ (yeast FKBP12 homolog) to reduce
1059 competition between for binding of Frb and Fkbp12. **C.** Same as in (A) but for wild type
1060 (UB27083) and *WHI5-AA* (UB25431) collected at 2 h in SPO. **D.** Same as in (A) but for
1061 wild type (UB27083) and Δ*LUTI; WHI5-AA* (UB25428) collected at 2 h in SPO. **E.** Live-
1062 cell imaging of cells in meiosis marked by Rec8-GFP and nuclear marker Htb1-mCherry.
1063 The following genotypes were imaged: wild type (UB35987), Δ*LUTI* (UB35989), *WHI5-*
1064 *AA* (UB35991), Δ*LUTI; WHI5-AA* (UB35989)**.** Quantification as percent of cells that
1065 entered meiosis assayed by nuclear Rec8 appearance. Experiments were performed
1066 using two biological replicates, mean value plotted with range. Differences in meiotic
1067 progression compared by Mann-Whitney test, two-tailed (*, p = 0.0112 [wild type vs.
1068 Δ*LUTI*; *WHI5-AA*]). **F.** Model of SBF regulation during meiotic entry. Ime1 downregulates
1069 Swi4 protein expression via induction of $SWI4^{LUTI}$ while Whi5 represses SBF activity in
1070 parallel to LUTI-based mechanism to prevent expression of SBF targets, including G1
1071 cyclins, which perturb meiotic entry via blocking interaction between Ime1 and its cofactor
1072 Ume6.

1073

1074
1075
1076

1077 **REFERENCES**
1078

1079 Abeliovich, H., and D.J. Klionsky. 2001. Autophagy in Yeast: Mechanistic Insights and
1080 Physiological Function. *Microbiol. Mol. Biol. Rev.* 65:463–479.
1081 doi:10.1128/mmbr.65.3.463-479.2001.
1082 Andrews, B.J., and I. Herskowitz. 1989. The yeast SWI4 protein contains a motif
1083 present in developmental regulators and is part of a complex involved in cell-cycle-
1084 dependent transcription. *Nature*. 342:830–833. doi:10.1038/342830a0.
1085 Argüello-Miranda, O., Y. Liu, N.E. Wood, P. Kositangool, and A. Doncic. 2018.
1086 Integration of Multiple Metabolic Signals Determines Cell Fate Prior to
1087 Commitment. *Mol. Cell*. 71:733-744.e11. doi:10.1016/j.molcel.2018.07.041.
1088 Bähler, J., J.Q. Wu, M.S. Longtine, N.G. Shah, A. McKenzie, A.B. Steever, A. Wach, P.
1089 Philippsen, and J.R. Pringle. 1998. Heterologous modules for efficient and versatile
1090 PCR-based gene targeting in Schizosaccharomyces pombe. *Yeast*. 14:943–951.
1091 doi:10.1002/(SICI)1097-0061(199807)14:10<943::AID-YEA292>3.0.CO;2-Y.
1092 Bean, J.M., E.D. Siggia, and F.R. Cross. 2005. High functional overlap between MluI
1093 cell-cycle box binding factor and Swi4/6 cell-cycle box binding factor in the G1/S
1094 transcriptional program in Saccharomyces cerevisiae. *Genetics*. 171:49–61.
1095 doi:10.1534/genetics.105.044560.
1096 Berchowitz, L.E., A.S. Gajadhar, F.J. van Werven, A.A. De Rosa, M.L. Samoylova, G.A.
1097 Brar, Y. Xu, C. Xiao, B. Futcher, J.S. Weissman, F.M. White, and A. Amon. 2013. A
1098 developmentally regulated translational control pathway establishes the meiotic
1099 chromosome segregation pattern. *Genes Dev.* 27:2147–2163.
1100 doi:10.1101/gad.224253.113.
1101 Bowdish, K.S., H.E. Yuan, and A.P. Mitchell. 1994. Analysis of RIM11, a yeast protein
1102 kinase that phosphorylates the meiotic activator IME1. *Mol. Cell. Biol.* 14:7909–
1103 7919. doi:10.1128/mcb.14.12.7909-7919.1994.
1104 Bowdish, K.S., H.E. Yuan, and A.P. Mitchell. 1995. Positive control of yeast meiotic
1105 genes by the negative regulator UME6. *Mol. Cell. Biol.* 15:2955–2961.
1106 doi:10.1128/mcb.15.6.2955.
1107 Brar, G.A., M. Yassour, N. Friedman, A. Regev, N.T. Ingolia, and J.S. Weissman. 2012.
1108 High-Resolution View of the Yeast Meiotic Program Revealed by Ribosome

1109 Profiling. *Science (80-.).* 335:552–558. doi:10.1126/science.1215110.
1110 Breitkreutz, A., H. Choi, J.R. Sharom, L. Boucher, V. Neduva, B. Larsen, Z.Y. Lin, B.J.
1111 Breitkreutz, C. Stark, G. Liu, J. Ahn, D. Dewar-Darch, T. Reguly, X. Tang, R.
1112 Almeida, Z.S. Qin, T. Pawson, A.C. Gingras, A.I. Nesvizhskii, and M. Tyers. 2010.
1113 A global protein kinase and phosphatase interaction network in yeast. *Science (80-.*
1114 *).* 328:1043–1046. doi:10.1126/science.1176495.
1115 De Bruin, R.A.M., W.H. McDonald, T.I. Kalashnikova, J. Yates, and C. Wittenberg.
1116 2004. Cln3 activates G1-specific transcription via phosphorylation of the SBF
1117 bound repressor Whi5. *Cell*. 117:887–898. doi:10.1016/j.cell.2004.05.025.
1118 Brush, G.S., N.A. Najor, A.A. Dombkowski, D. Cukovic, and K.E. Sawarynski. 2012.
1119 Yeast ime2 functions early in meiosis upstream of cell cycle-regulated sbf and mbf
1120 targets. *PLoS One*. 7:1–12. doi:10.1371/journal.pone.0031575.
1121 Carlile, T.M., and A. Amon. 2008. Meiosis I Is Established through Division-Specific
1122 Translational Control of a Cyclin. *Cell*. 133:280–291.
1123 doi:10.1016/j.cell.2008.02.032.
1124 Chen, J., D. Mcswiggen, and E. Ünal. 2018. Single Molecule Fluorescence In Situ
1125 Hybridization (smFISH) Analysis in Budding Yeast Vegetative Growth and
1126 Meiosis. 1–14. doi:10.3791/57774.
1127 Chen, J., A. Tresenrider, M. Chia, D.T. McSwiggen, G. Spedale, V. Jorgensen, H. Liao,
1128 F.J. Van Werven, and E. Ünal. 2017. Kinetochore inactivation by expression of a
1129 repressive mRNA. *Elife*. 6:1–31. doi:10.7554/eLife.27417.
1130 Cheng, Z., G.M. Otto, E.N. Powers, A. Keskin, P. Mertins, S.A. Carr, M. Jovanovic, and
1131 G.A. Brar. 2018. Pervasive, Coordinated Protein-Level Changes Driven by
1132 Transcript Isoform Switching during Meiosis. *Cell*. 172:910-923.e16.
1133 doi:10.1016/j.cell.2018.01.035.
1134 Chia, M., A. Tresenrider, J. Chen, G. Spedale, V. Jorgensen, E. Ünal, and F.J. van
1135 Werven. 2017. Transcription of a 5’ extended mRNA isoform directs dynamic
1136 chromatin changes and interference of a downstream promoter. *Elife*. 6:1–23.
1137 doi:10.7554/eLife.27420.
1138 Chia, M., and F.J. van Werven. 2016. Temporal Expression of a Master Regulator
1139 Drives Synchronous Sporulation in Budding Yeast. *G3:*

1140 *Genes|Genomes|Genetics*. 6:3553–3560. doi:10.1534/g3.116.034983.
1141 Colomina, N., E. Garí, C. Gallego, E. Herrero, and M. Aldea. 1999. G1cyclins block the
1142 Ime1 pathway to make mitosis and meiosis incompatible in budding yeast. *EMBO*
1143 *J.* 18:320–329. doi:10.1093/emboj/18.2.320.
1144 Costanzo, M., J.L. Nishikawa, X. Tang, J.S. Millman, O. Schub, K. Breitkreuz, D. Dewar,
1145 I. Rupes, B. Andrews, and M. Tyers. 2004. CDK activity antagonizes Whi5, an
1146 inhibitor of G1/S transcription in yeast. *Cell*. 117:899–913.
1147 doi:10.1016/j.cell.2004.05.024.
1148 Van Dalfsen, K.M., S. Hodapp, A. Keskin, G.M. Otto, C.A. Berdan, A. Higdon, T.
1149 Cheunkarndee, D.K. Nomura, M. Jovanovic, and G.A. Brar. 2018. Global Proteome
1150 Remodeling during ER Stress Involves Hac1-Driven Expression of Long
1151 Undecoded Transcript Isoforms. *Dev. Cell*. 46:219-235.e8.
1152 doi:10.1016/j.devcel.2018.06.016.
1153 Dorsey, S., S. Tollis, J. Cheng, L. Black, S. Notley, M. Tyers, and C.A. Royer. 2018.
1154 G1/S Transcription Factor Copy Number Is a Growth-Dependent Determinant of
1155 Cell Cycle Commitment in Yeast. *Cell Syst.* 6:539-554.e11.
1156 doi:10.1016/j.cels.2018.04.012.
1157 Eisenberg, A.R., A.L. Higdon, I. Hollerer, A.P. Fields, I. Jungreis, P.D. Diamond, M.
1158 Kellis, M. Jovanovic, and G.A. Brar. 2020. Translation Initiation Site Profiling
1159 Reveals Widespread Synthesis of Non-AUG-Initiated Protein Isoforms in Yeast.
1160 *Cell Syst.* 11:145-160.e5. doi:10.1016/j.cels.2020.06.011.
1161 Espinoza, F.H., J. Ogas, I. Herskowitz, and D. Morgant. 2016. Cell Cycle Control by a
1162 Complex of the Cyclin HCS26 (PCL1) and the Kinase PHO85 Author (s): F .
1163 Hernan Espinoza , Joseph Ogas , Ira Herskowitz and David O . Morgan Published
1164 by : American Association for the Advancement of Science Stable URL : http://.
1165 266:1388–1391.
1166 Fridy, P.C., Y. Li, S. Keegan, M.K. Thompson, I. Nudelman, J.F. Scheid, M. Oeffinger,
1167 M.C. Nussenzweig, D. Fenyö, B.T. Chait, and M.P. Rout. 2014. A robust pipeline
1168 for rapid production of versatile nanobody repertoires. *Nat. Methods*. 11:1253–
1169 1260. doi:10.1038/nmeth.3170.
1170 Gallego, C., E. Garí, N. Colomina, E. Herrero, and M. Aldea. 1997. The Cln3 cyclin is

1171 down-regulated by translational repression and degradation during the G1 arrest
1172 caused by nitrogen deprivation in budding yeast. *EMBO J.* 16:7196–7206.
1173 doi:10.1093/emboj/16.23.7196.
1174 Gaubatz, S., G.J. Lindeman, S. Ishida, L. Jakoi, J.R. Nevins, D.M. Livingston, and R.E.
1175 Rempel. 2000. E2F4 and E2F5 play an essential role in pocket protein-mediated
1176 G1 control. *Mol. Cell*. 6:729–735. doi:10.1016/S1097-2765(00)00071-X.
1177 Gibson, D.G., L. Young, R.Y. Chuang, J.C. Venter, C.A. Hutchison, and H.O. Smith.
1178 2009. Enzymatic assembly of DNA molecules up to several hundred kilobases. *Nat.*
1179 *Methods*. 6:343–345. doi:10.1038/nmeth.1318.
1180 Harris, M.R., D. Lee, S. Farmer, N.F. Lowndes, and R.A.M. de Bruin. 2013. Binding
1181 Specificity of the G1/S Transcriptional Regulators in Budding Yeast. *PLoS One*.
1182 8:1–7. doi:10.1371/journal.pone.0061059.
1183 Hartwell, L.H., J. Culotti, J.R. Pringle, and B.J. Reid. 1974. Genetic control of the cell
1184 division cycle in yeast. *Science*. 183:46–51. doi:10.1126/SCIENCE.183.4120.46.
1185 Haruki, H., J. Nishikawa, and U.K. Laemmli. 2008. The Anchor-Away Technique: Rapid,
1186 Conditional Establishment of Yeast Mutant Phenotypes. *Mol. Cell*. 31:925–932.
1187 doi:10.1016/j.molcel.2008.07.020.
1188 Hasan, M., S. Brocca, E. Sacco, M. Spinelli, P. Elena, L. Matteo, A. Lilia, and M.
1189 Vanoni. 2014. A comparative study of Whi5 and retinoblastoma proteins : from
1190 sequence and structure analysis to intracellular networks. 4:1–24.
1191 doi:10.3389/fphys.2013.00315.
1192 Van Den Heuvel, S., and N.J. Dyson. 2008. Conserved functions of the pRB and E2F
1193 families. *Nat. Rev. Mol. Cell Biol.* 9:713–724. doi:10.1038/nrm2469.
1194 Hollerer, I., J.C. Barker, V. Jorgensen, A. Tresenrider, C. Dugast-Darzacq, L.Y. Chan,
1195 X. Darzacq, R. Tjian, E. Ünal, and G.A. Brar. 2019. Evidence for an integrated gene
1196 repression mechanism based on mRNA isoform toggling in human cells. *G3*
1197 *Genes, Genomes, Genet.* 9:1045–1053. doi:10.1534/g3.118.200802.
1198 Holt, L., B. Tuch, J. Villén, A. Johnson, S. Gygi, and D. Morgan. 2009. Global analysis
1199 of Cdk1 substrate phosphorylation sites provides insights into evolution. *Science*
1200 *(80-.).* 325:1682–1686.
1201 Honigberg, S.M. 2003. Signal pathway integration in the switch from the mitotic cell

1202 cycle to meiosis in yeast. *J. Cell Sci.* 116:2137–2147. doi:10.1242/jcs.00460.
1203 Iyer, V.R., C.E. Horak, P.O. Brown, D. Botstein, V.R. Iyer, M. Snyder, and C.S. Scafe.
1204 2001. Genomic binding sites of the yeast cell-cycle transcription factors SBF and
1205 MBF. *Nature*. 409:533–538. doi:10.1038/35054095.
1206 Johnston, G.C., J.R. Pringle, and L.H. Hartwell. 1977. Coordination of Growth With Cell
1207 Division. *Exp. Cell Res.* 105:79–98.
1208 Jorgensen, P., and M. Tyers. 2004. How cells coordinate growth and division. *Curr. Biol.*
1209 14:1014–1027. doi:10.1016/j.cub.2004.11.027.
1210 Julian, L.M., Y. Liu, C.A. Pakenham, D. Dugal-Tessier, V. Ruzhynsky, S. Bae, S.Y. Tsai,
1211 G. Leone, R.S. Slack, and A. Blais. 2016. Tissue-specific targeting of cell fate
1212 regulatory genes by E2f factors. *Cell Death Differ.* 23:565–575.
1213 doi:10.1038/cdd.2015.36.
1214 Kadosh, D., and K. Struhl. 1997. Repression by Ume6 involves recruitment of a
1215 complex containing Sin3 corepressor and Rpd3 histone deacetylase to target
1216 promoters. *Cell*. 89:365–371. doi:10.1016/S0092-8674(00)80217-2.
1217 Kassir, Y., D. Granot, and G. Simchen. 1988. IME1, a positive regulator gene of meiosis
1218 in S. cerevisiae. *Cell*. 52:853–862. doi:10.1016/0092-8674(88)90427-8.
1219 Kelliher, C.M., M.W. Foster, F.C. Motta, A. Deckard, E.J. Soderblom, M.A. Moseley, and
1220 S.B. Haase. 2018. Layers of regulation on cell-cycle gene expression in the
1221 budding yeast *Saccharomyces cerevisiae*. *Mol. Biol. Cell*. mbc.E18-04-0255.
1222 doi:10.1091/mbc.E18-04-0255.
1223 Kim, D., J.M. Paggi, C. Park, C. Bennett, and S.L. Salzberg. 2019. Graph-based
1224 genome alignment and genotyping with HISAT2 and HISAT-genotype. *Nat.*
1225 *Biotechnol.* 37:907–915. doi:10.1038/s41587-019-0201-4.
1226 Klein, F., P. Mahr, M. Galova, S.B.C. Buonomo, C. Michaelis, K. Nairz, and K. Nasmyth.
1227 1999. A Central Role for Cohesins in Sister Chromatid Cohesion, Formation of
1228 Axial Elements, and Recombination during Yeast Meiosis Genetic and biochemical
1229 analyses have identified. *Cell*. 98:91–103.
1230 Love, M.I., W. Huber, and S. Anders. 2014. Moderated estimation of fold change and
1231 dispersion for RNA-seq data with DESeq2. *Genome Biol.* 15:1–21.
1232 doi:10.1186/s13059-014-0550-8.

1233 Malathi, K., Y. Xiao, and A.P. Mitchell. 1997. Interaction of yeast repressor-activator
1234 protein Ume6p with glycogen synthase kinase 3 homolog Rim11p. *Mol. Cell. Biol.*
1235 17:7230–7236. doi:10.1128/mcb.17.12.7230.
1236 Malathi, K., Y. Xiao, and A.P. Mitchell. 1999. Catalytic roles of yeast GSK3β/shaggy
1237 homolog Rim11p in meiotic activation. *Genetics*. 153:1145–1152.
1238 doi:10.1093/genetics/153.3.1145.
1239 Mcinerny, C.J., J.F. Partridge, G.E. Mikesell, D.P. Creemer, and L.L. Breeden. 1997. A
1240 novel Mcml-dependent element in the WI4 , CLN3 , CDC6 , and CDC4S7
1241 promoters activates M / Gi-specific transcription. *Genes Dev.* 1277–1288.
1242 doi:10.1101/gad.11.10.1277.
1243 Miller, M.P., E. Ünal, G.A. Brar, and A. Amon. 2012. Meiosis I chromosome segregation
1244 is established through regulation of microtubule-kinetochore interactions. *Elife*.
1245 2012:1–30. doi:10.7554/eLife.00117.
1246 Moreno-Torres, M., M. Jaquenoud, M.P. Péli-Gulli, R. Nicastro, and C. De Virgilio. 2017.
1247 TORC1 coordinates the conversion of Sic1 from a target to an inhibitor of cyclin-
1248 CDK-Cks1. *Cell Discov.* 3:1–12. doi:10.1038/celldisc.2017.12.
1249 Parviz, F., and W. Heideman. 1998. Growth-independent regulation of CLN3 mRNA
1250 levels by nutrients in Saccharomyces cerevisiae. *J. Bacteriol.* 180:225–230.
1251 doi:10.1128/jb.180.2.225-230.1998.
1252 Pertea, M., G.M. Pertea, C.M. Antonescu, T.C. Chang, J.T. Mendell, and S.L. Salzberg.
1253 2015. StringTie enables improved reconstruction of a transcriptome from RNA-seq
1254 reads. *Nat. Biotechnol.* 33:290–295. doi:10.1038/nbt.3122.
1255 Pnueli, L., I. Edry, M. Cohen, and Y. Kassir. 2004. Glucose and Nitrogen Regulate the
1256 Switch from Histone Deacetylation to Acetylation for Expression of Early Meiosis-
1257 Specific Genes in Budding Yeast. *Mol. Cell. Biol.* 24:5197–5208.
1258 doi:10.1128/mcb.24.12.5197-5208.2004.
1259 Primig, M., R.M. Williams, E.A. Winzeler, G.G. Tevzadze, A.R. Conway, S.Y. Hwang,
1260 R.W. Davis, and R.E. Esposito. 2000. The core meiotic transcriptome in budding
1261 yeasts. *Nat. Genet.* 26:415–423. doi:10.1038/82539.
1262 Raj, A., P. van den Bogaard, S.A. Rifkin, A. van Oudenaarden, and S. Tyagi. 2008.
1263 Imaging individual mRNA molecules using multiple singly labeled probes. *Nat.*

1264 *Methods*. 5:877–879. doi:10.1038/nmeth.1253.
1265 Rubin-Bejerano, I., S. Mandel, K. Robzyk, and Y. Kassir. 1996. Induction of meiosis in
1266 Saccharomyces cerevisiae depends on conversion of the transcriptional represssor
1267 Ume6 to a positive regulator by its regulated association with the transcriptional
1268 activator Ime1. *Mol. Cell. Biol.* 16:2518–2526. doi:10.1128/mcb.16.5.2518.
1269 Rundlett E., S., A. Carmen A., N. Suka, B. Turner M., and M. Grunstein. 2003.
1270 Transcriptional repression byUME6 involves deacetylationof lysine5 of
1271 histoneH4byRPD3. *Nature*. 426:181–186.
1272 Schindelin, J., I. Arganda-Carreras, E. Frise, V. Kaynig, M. Longair, T. Pietzsch, S.
1273 Preibisch, C. Rueden, S. Saalfeld, B. Schmid, J.Y. Tinevez, D.J. White, V.
1274 Hartenstein, K. Eliceiri, P. Tomancak, and A. Cardona. 2012. Fiji: An open-source
1275 platform for biological-image analysis. *Nat. Methods*. 9:676–682.
1276 doi:10.1038/nmeth.2019.
1277 Sidorova, J.M., and L.L. Breeden. 2002. Precocious S-phase entry in budding yeast
1278 prolongs replicative state and increases dependence upon Rad53 for viability.
1279 *Genetics*. 160:123–136.
1280 Simon, I., J. Barnett, N. Hannett, C.T. Harbison, N.J. Rinaldi, T.L. Volkert, J.J. Wyrick, J.
1281 Zeitlinger, D.K. Gifford, T.S. Jaakkola, and R.A. Young. 2001. Serial Regulation of
1282 Transcriptional Regulators in the Yeast Cell Cycle. 106:697–708.
1283 Smith, H.E., S.E. Driscoll, R.A.L. Sia, H.E. Yuan, and A.P. Mitchell. 1993. Genetic
1284 evidence for transcriptional activation by the yeast IME1 gene product. *Genetics*.
1285 133:775–784. doi:10.1093/genetics/133.4.775.
1286 Smolka, M.B., F.M. Bastos De Oliveira, M.R. Harris, and R.A.M. De Bruin. 2012. The
1287 checkpoint transcriptional response: Make sure to turn it off once you are satisfied.
1288 *Cell Cycle*. 11:3166–3174. doi:10.4161/cc.21197.
1289 Spellman, P., G. Sherlock, M. Zhang, V. Iyer, K. Anders, M. Eisen, P. Brown, D.
1290 Botstein, and B. Futcher. 1998. Comprehensive identification of cell cycle-regulated
1291 genes of the yeast Saccharomyces cerevisiae by microarray hybridization. *Mol.*
1292 *Biol. Cell*. 9:3273–3297. doi:10.1091/mbc.9.12.3273.
1293 Subramanian, A., P. Tamayo, V.K. Mootha, S. Mukherjee, B.L. Ebert, M.A. Gillette, A.
1294 Paulovich, S.L. Pomeroy, T.R. Golub, E.S. Lander, and J.P. Mesirov. 2005. Gene

1295 set enrichment analysis: A knowledge-based approach for interpreting genome-
1296 wide expression profiles. *Proc. Natl. Acad. Sci. U. S. A.* 102:15545–15550.
1297 doi:10.1073/pnas.0506580102.
1298 Talarek, N., E. Cameroni, M. Jaquenoud, X. Luo, S. Bontron, S. Lippman, G. Devgan,
1299 M. Snyder, J.R. Broach, and C. De Virgilio. 2010. Initiation of the TORC1-
1300 Regulated G0 Program Requires Igo1/2, which License Specific mRNAs to Evade
1301 Degradation via the 5′-3′ mRNA Decay Pathway. *Mol. Cell*. 38:345–355.
1302 doi:10.1016/j.molcel.2010.02.039.
1303 Tresenrider, A., K. Morse, V. Jorgensen, M. Chia, H. Liao, F.J. van Werven, and E.
1304 Ünal. 2021. Integrated genomic analysis reveals key features of long undecoded
1305 transcript isoform-based gene repression. *Mol. Cell*. 81:2231-2245.e11.
1306 doi:10.1016/j.molcel.2021.03.013.
1307 Tresenrider, A., and E. Ünal. 2017. One-two punch mechanism of gene repression: a
1308 fresh perspective on gene regulation. *Curr. Genet.* 0:1–8. doi:10.1007/s00294-017-
1309 0793-5.
1310 Vidan, S., and A.P. Mitchell. 1997. Stimulation of yeast meiotic gene expression by the
1311 glucose-repressible protein kinase Rim15p. *Mol. Cell. Biol.* 17:2688–2697.
1312 doi:10.1128/mcb.17.5.2688.
1313 Wagner, M. V., M.B. Smolka, R.A.M. de Bruin, H. Zhou, C. Wittenberg, and S.F. Dowdy.
1314 2009. Whi5 regulation by site specific CDK-phosphorylation in Saccharomyces
1315 cerevisiae. *PLoS One*. 4. doi:10.1371/journal.pone.0004300.
1316 Vander Wende, H.M., M. Gopi, M. Onyundo, C. Medrano, T. Adanlawo, and G.A. Brar.
1317 2022. Meiotic resetting of the cellular Sod1 pool is driven by protein aggregation,
1318 degradation, and transient LUTI-mediated repression. *J. Cell Biol.* 222.
1319 doi:10.1101/2022.06.28.498006.
1320 van Werven, F.J., and A. Amon. 2011. Regulation of entry into gametogenesis. *Philos.*
1321 *Trans. R. Soc. B Biol. Sci.* 366:3521–3531. doi:10.1098/rstb.2011.0081.
1322
1323
1324

Figure 1

Su et al_Figure 1

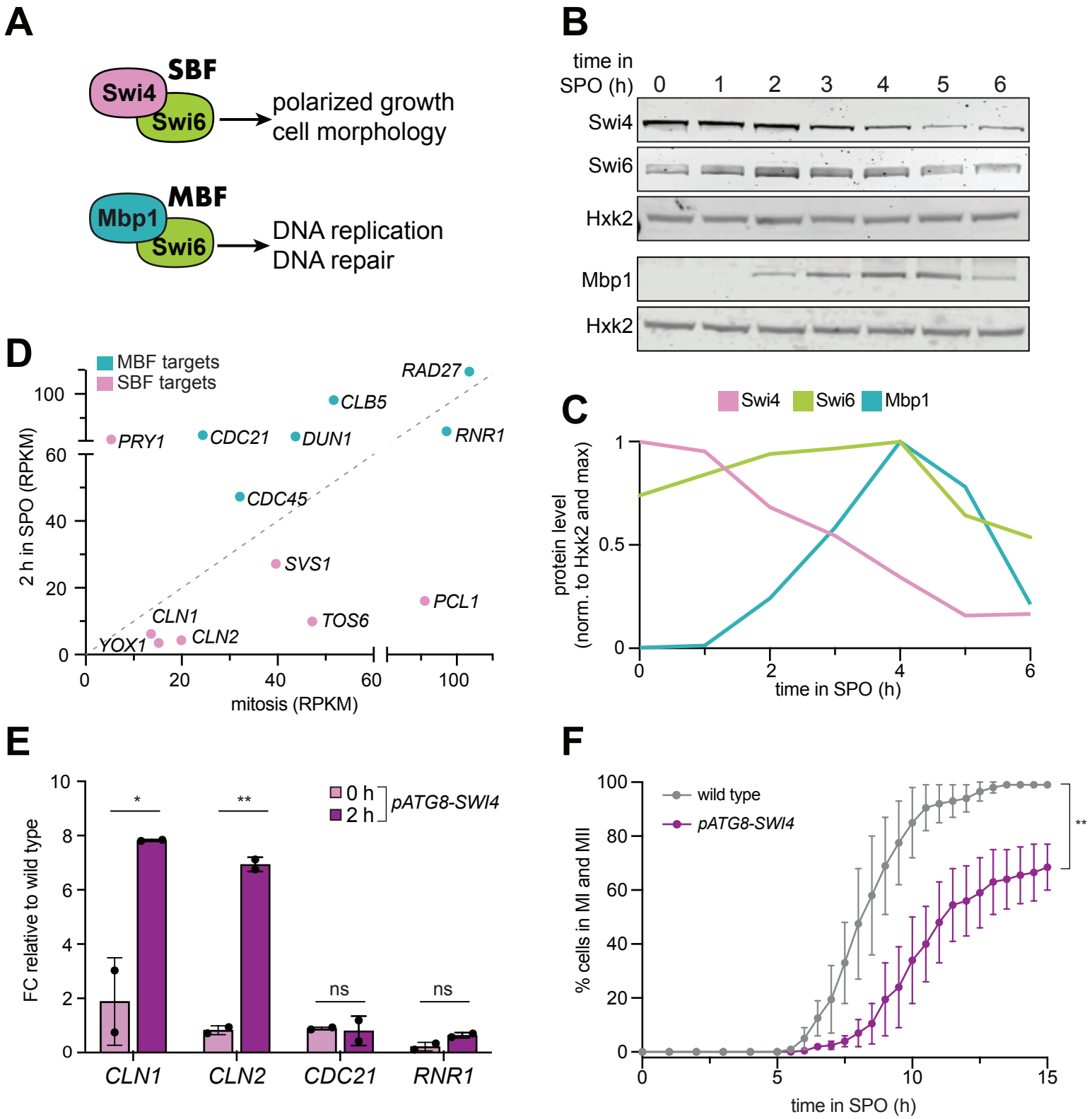

Figure 2

Su et al_Figure 2

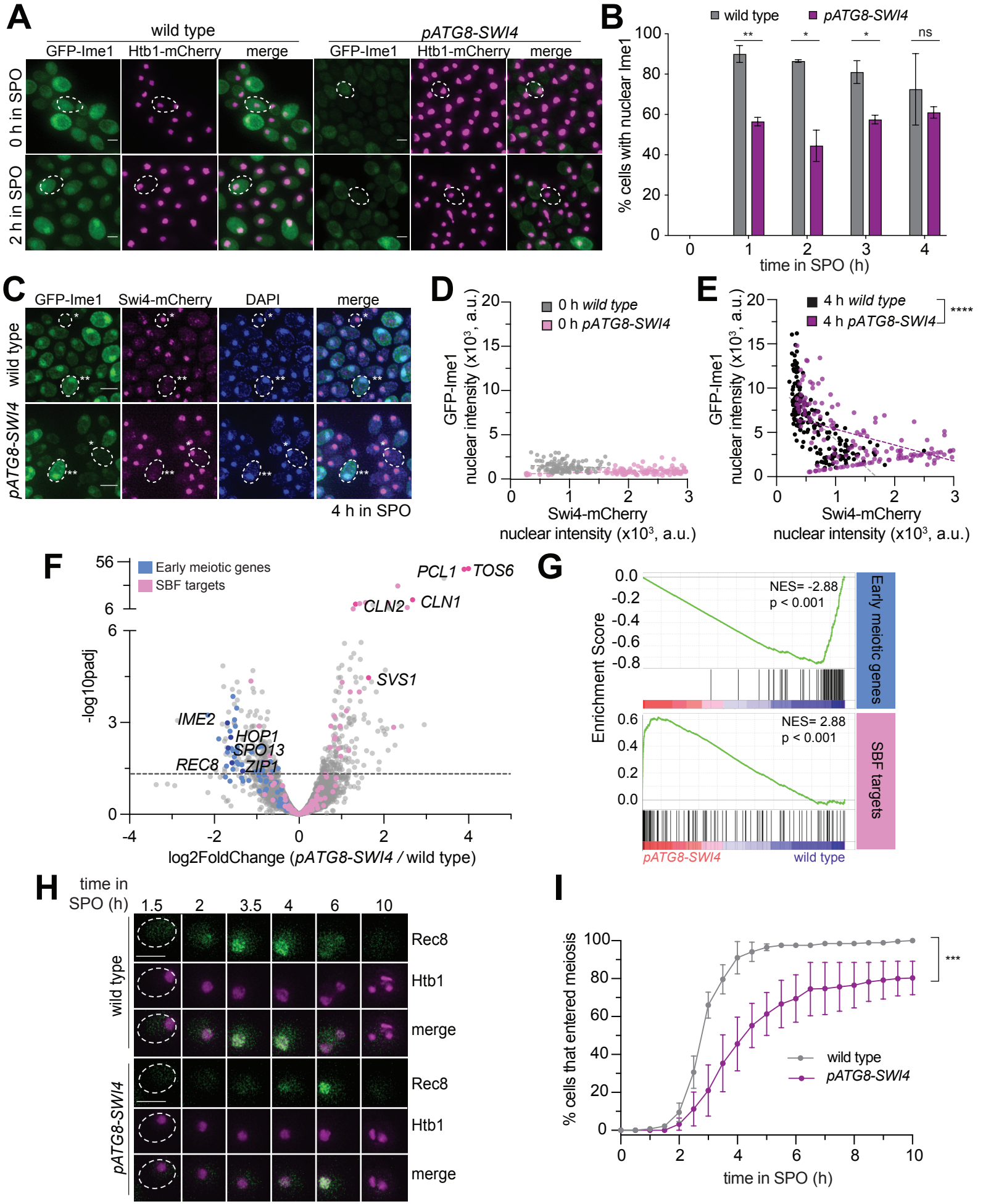

Figure 3

Su et al_Figure 3

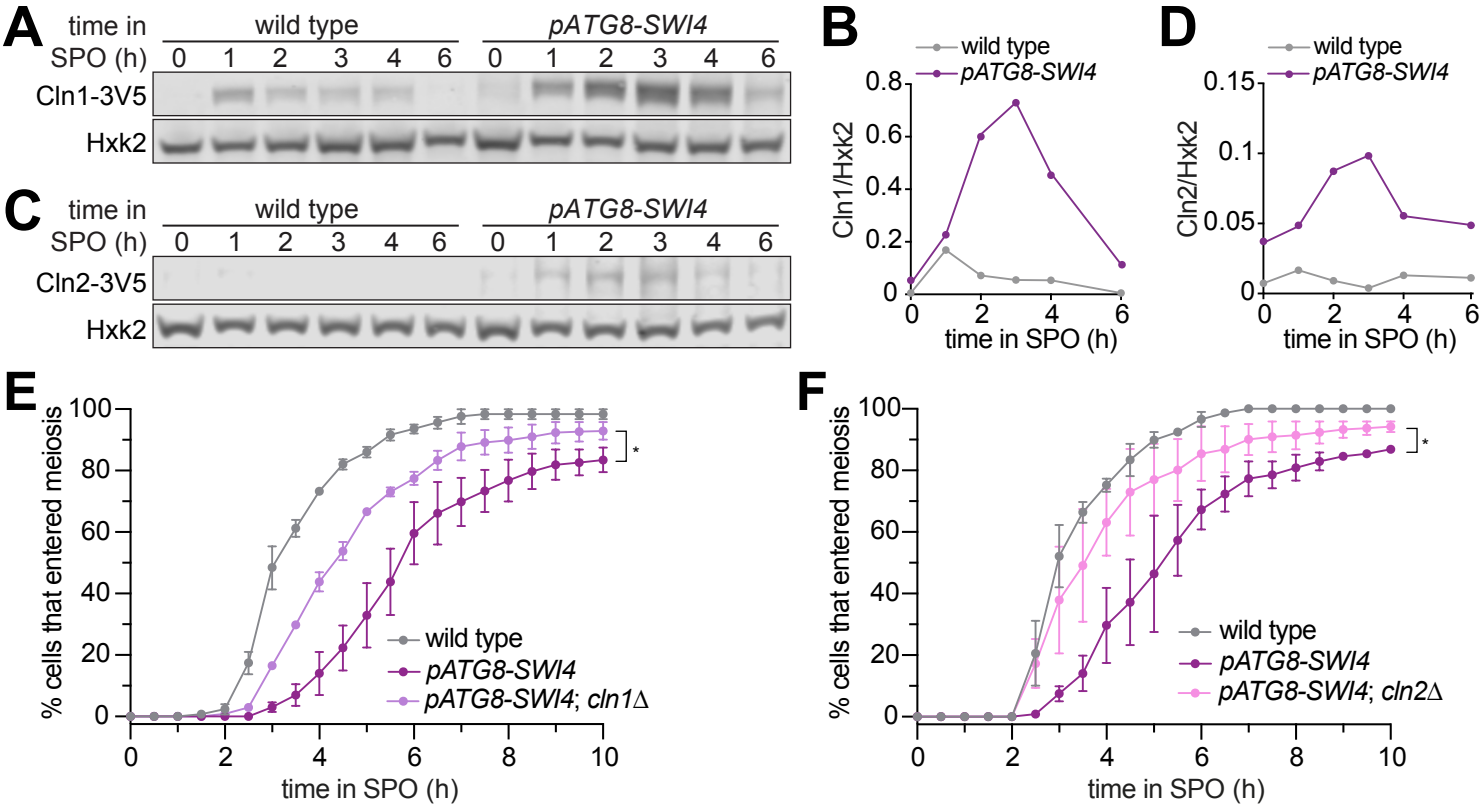

Figure 4

Su et al_Figure 4

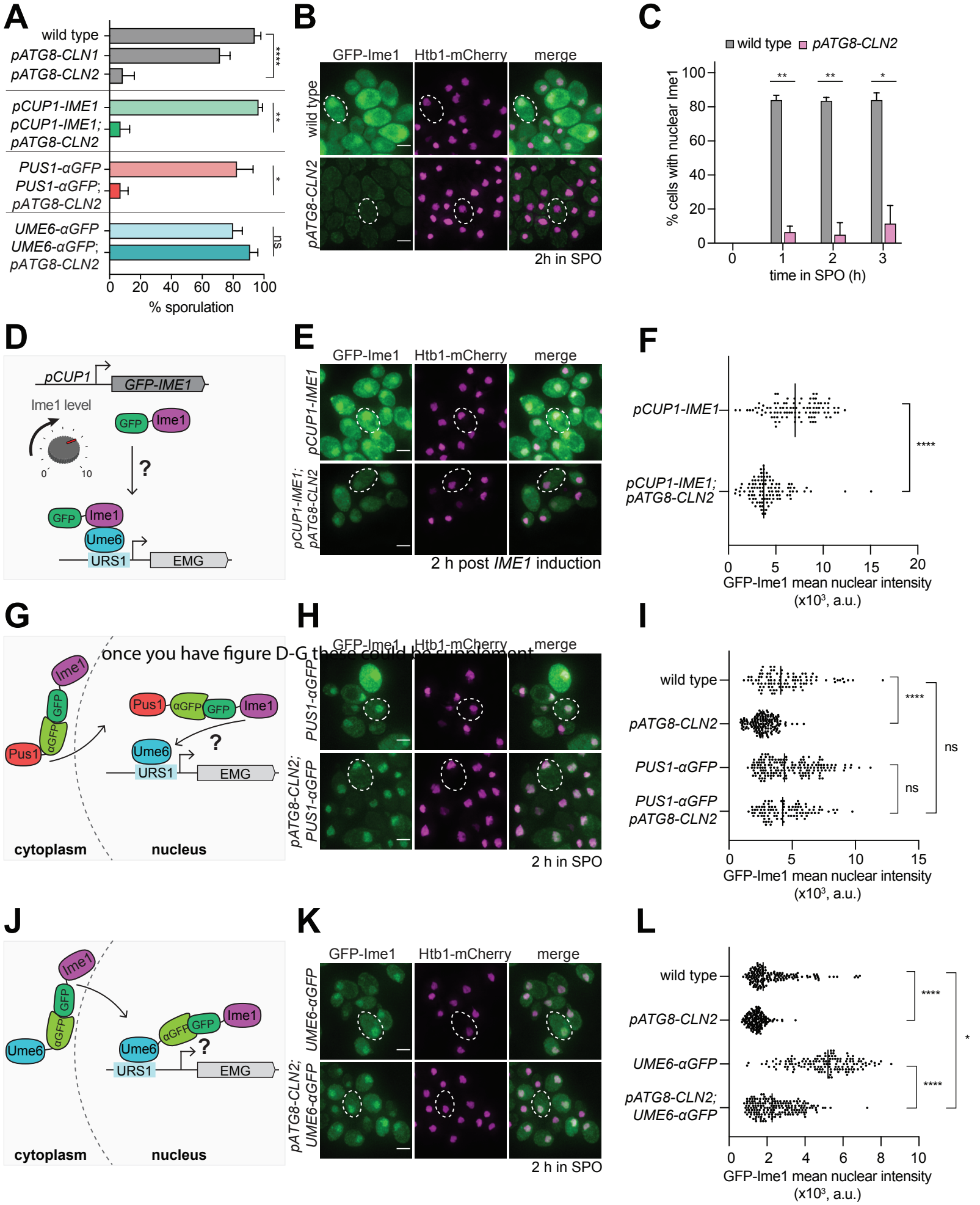

Figure 5

Su et al_Figure 5

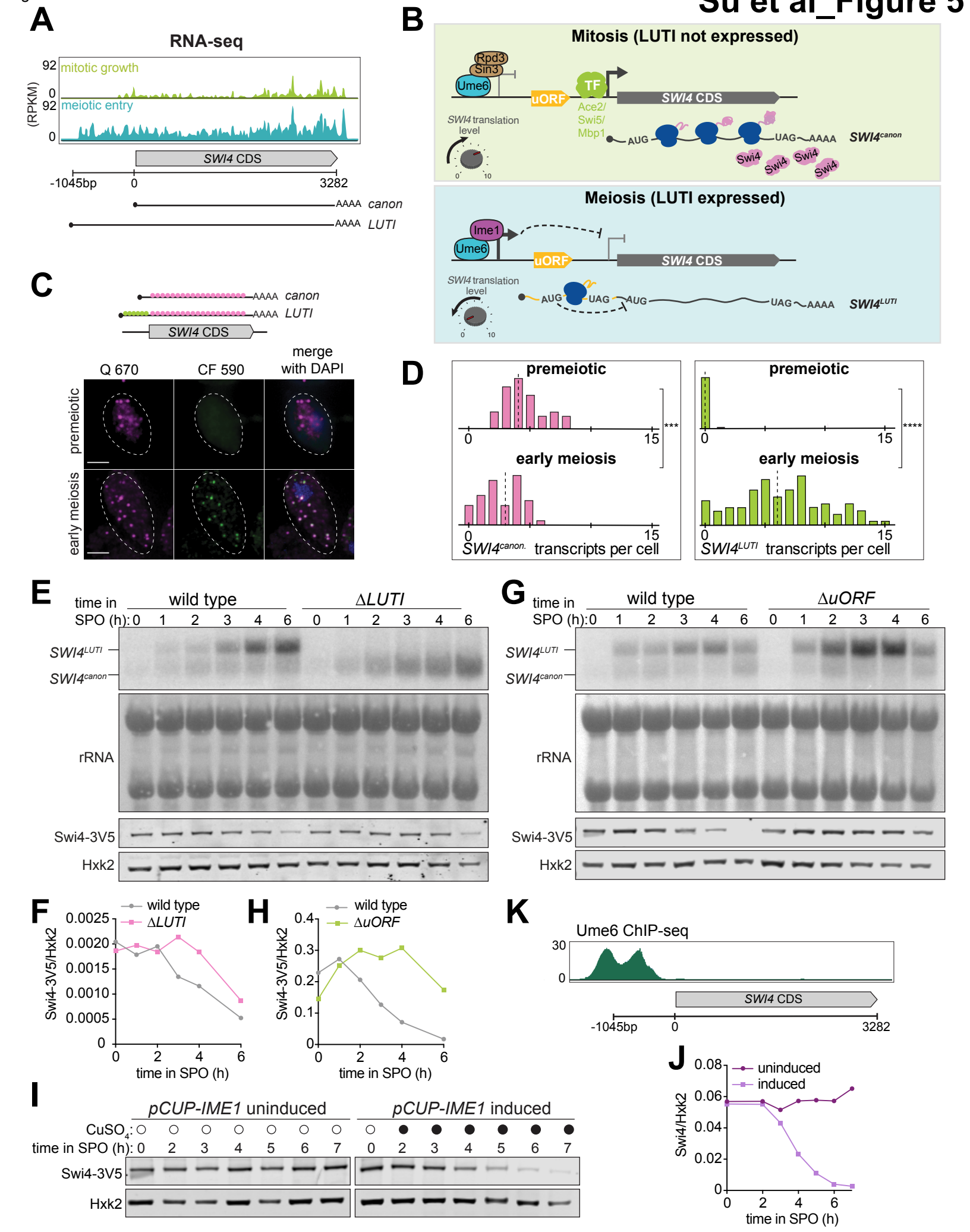

Figure 6

Su et al_Figure 6

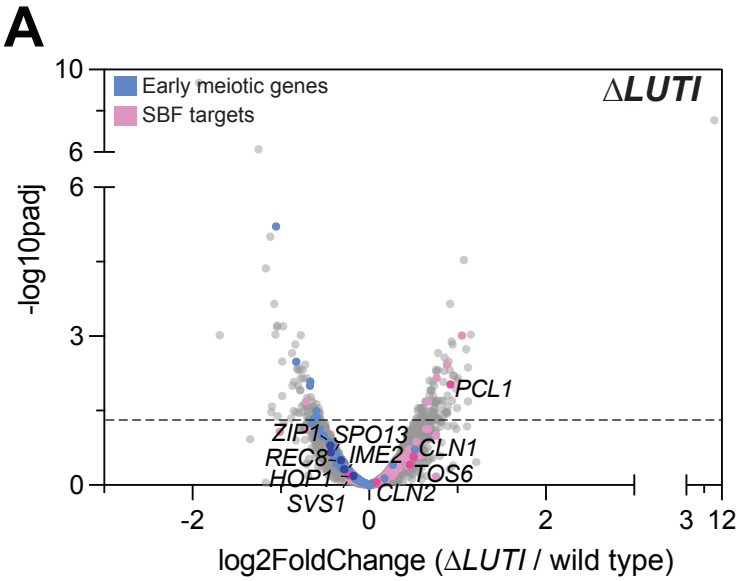

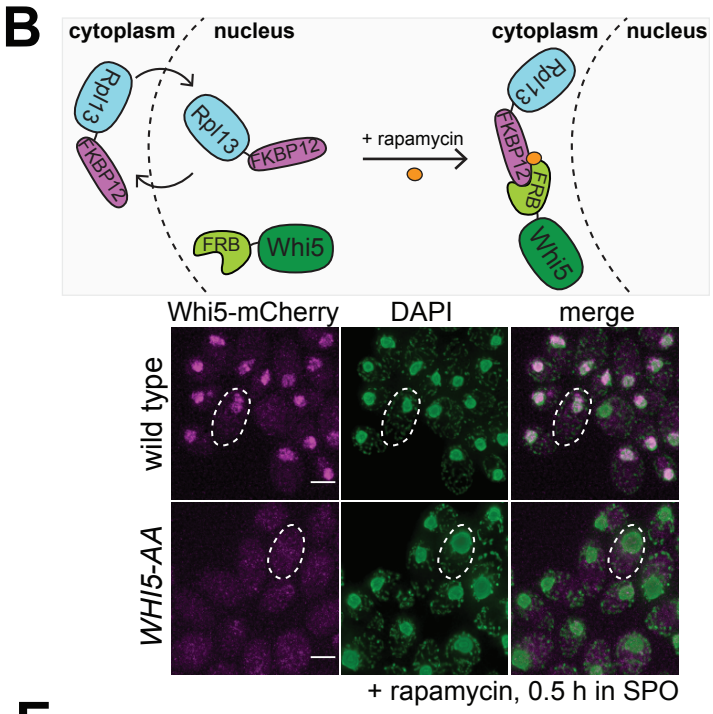

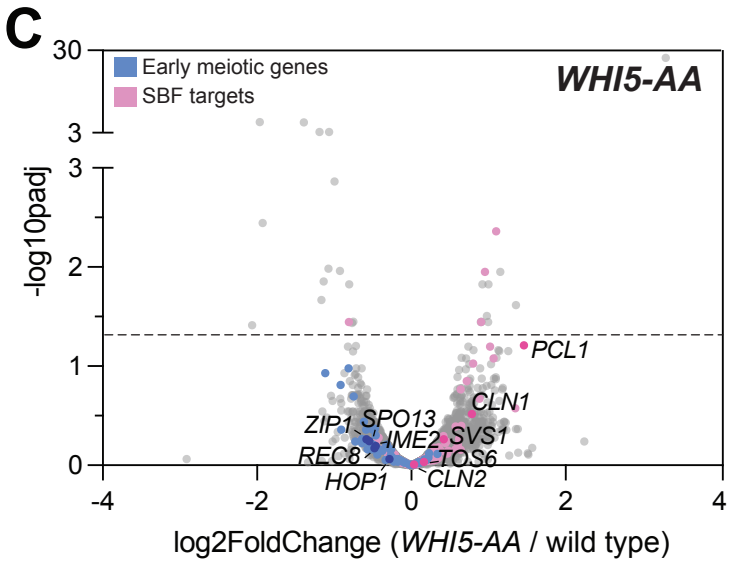

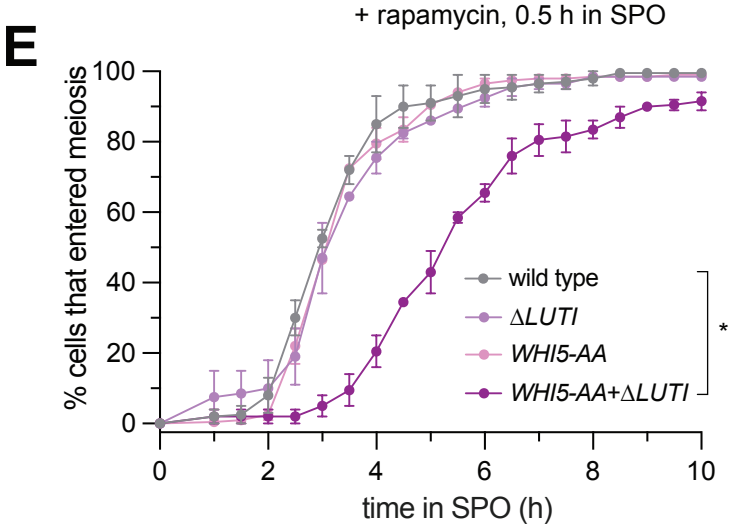

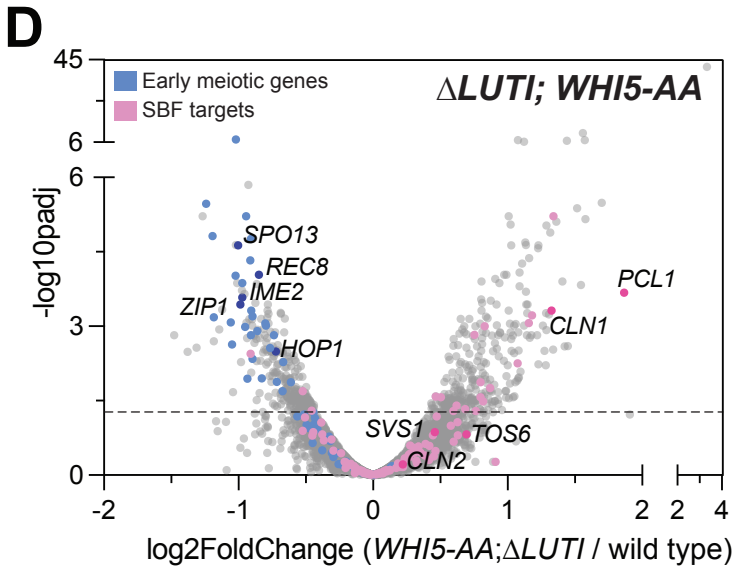

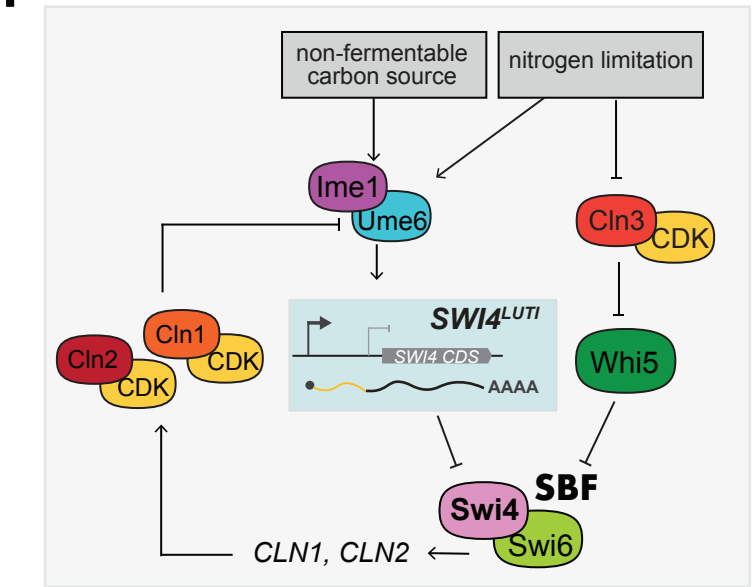

Supplemental Figure Legends

S1. Swi4 and Ime1 protein abundance, Related to Figure 1

A. Wild type (UB22199) and *pATG8-SWI4* (UB22226) cells collected between 0-4 h in SPO. Immunoblot performed using α-V5 to quantify Swi4-3V5 abundance. Normalized to Hxk2 loading control. **B.** Quantification of the immunoblot in (A). **C.** Immunoblot using α-GFP to quantify GFP-Ime1 abundance. Normalized to Hxk2 loading control. **D.** Quantification of the immunoblot in (C).

S2. Gene ontology analysis for mRNA-seq comparing *pATG8-SWI4* to wild type, Related to Figure 2

A. Gene ontology analysis for genes that have significant increased expression by DESeq2 (see Materials and Methods) in *pATG8-SWI4* (UB2226) and wild type (UB22199*)*. Term size is the number of genes within a defined term. Enrichment score calculated for each term and plotted. **B.** same as in (A) but for genes that have significant decreased expression.

S4. Ime1 protein levels when C*LN2* is overexpressed and rescue of I*ME1* transcript levels and protein abundance with *pCUP1-IME1*, Related to Figure 4

A. Immunoblot was performed on wild type (UB22199) and *pATG8-CLN2* (UB35106) cells collected between 0-6 h in SPO. Immunoblotted using α-GFP to quantify GFP-Ime1 abundance. Normalized to Hxk2 loading control. Representative blots from one of two biological replicates are shown. All blots in this figure were performed the same way. **B.** Quantification of the immunoblot in (A). **C.** RT-qPCR was performed on *IME1* transcript for samples collected in (A). Quantification was performed in reference to levels of meiotic housekeeping gene *PFY1* and then normalized to wild type. FC = fold change. Experiments were performed in duplicate, mean value plotted with range. **D.** Same as in (C) but for *pCUP1-GFP-IME1* (UB34641) and *pCUP1-GFP-IME1*; *pATG8-CLN2* (UB35057). **E.** Immunoblot was performed on samples from wild type (UB22199)*, pATG8-CLN2* (UB35106), *pCUP1-GFP-IME1* (UB34641), and *pCUP1-GFP-IME1*; *pATG8-CLN2* (UB35057) strains collected between 0-4 h in SPO. 50 μM $CuSO_4$ after 2 h in SPO was

added to all cells. Representative blots from one of two biological replicates are shown. **F.** Quantification of the immunoblot in (E).

S5. Expression of *SWI4^{LUTI}* in Ume6(T99N) mutant, Related to Figure 5

Fold change expression in wild type or Ume6(T99N) mutant between pre meiotic conditions and meiotic prophase (Tresenrider et al., 2021).

S6. Whi5 localization in early meiosis, Swi4 protein levels matching Figure 6A, 6C, 6D, and GSEA data for Δ*LUTI*; WHI5-AA, Related to Figure 6

A. Fixed imaging of cells marked with GFP-Ime1 and Whi5-mCherry with DNA stained with DAPI. Representative images with merge at 0 h and 2 h in SPO. Representative cells outlined. **B.** Left: Cells with the following genotypes were collected between 0-6 h in SPO: wild type (UB27083), Δ*LUTI* (UB26874), *WHI5-AA* (UB25431), Δ*LUTI; WHI5-AA* (UB25428). Immunoblotted using α-V5 to quantify Swi4-3V5 abundance. Normalized to Hxk2 loading control. Representative blots from one of two biological replicates are shown. Right: Quantification **C.** GSEA analysis of mRNA-seq comparing wildtype vs. Δ*LUTI; WHI5-AA (UB25428)* cells collected at 2 h in SPO. Vertical black bars represent early meiotic gene cluster from (Brar et al., 2012) or SBF cluster from (Iyer et al., 2001). The heatmap indicates genes that are more enriched in Δ*LUTI; WHI5-AA* (red, left-side) or genes that are enriched with wild type (blue, right-side). NES = normalized enrichment score. Enrichment was determined comparing wild type to Δ*LUTI; WHI5-AA.*

Supplement Table 1.

Table of differentially expressed genes (DESeq2) plotted in Figure 2F for *pATG8-SWI4* (UB22226) vs. wild type (UB22199).

Supplement Table 2.

Sporulation efficiency of cells at 24 h in SPO media for Rec8-GFP (UB32085*)*, Rec8-GFP; *pATG8-SWI4* (UB32089). 200 cells counted per strain. Second table is sporulation efficiency of cells at 24 h in SPO media for the following genotypes: wild type (UB22199), *pATG8-CLN1* (UB32820), *pATG8-CLN2* (UB25959), *pCUP-GFP-IME1* (UB34641),

pCUP1-GFP-IME1; pATG8-CLN2 (UB35057), *PUS1-αGFP* (UB35593), *PUS1-αGFP; pATG8-CLN2* (UB35982), *UME6-αGFP* (UB35300), and *UME6-αGFP; pATG8-CLN2* (UB35177).

Supplement Table 3.

Table of differentially expressed genes (DESeq2) plotted in Figure 6A, 6C, and 6D. First tab is *WHI5-AA*; Δ*LUTI* vs. wild type. Second tab is *WHI5-AA* vs. wild type. Third tab is Δ*LUTI* versus wild type.

Supplement Table 4.

The genotypes of the strains used in this study.

Supplement Table 5.

Plasmids used in this study.

Supplement Table 6.

Primers used for qPCR and RNA blotting in this study.

Supplemental Table 7.

Image acquisition information.

Figure 1 Supplement

Su et al_Figure S1

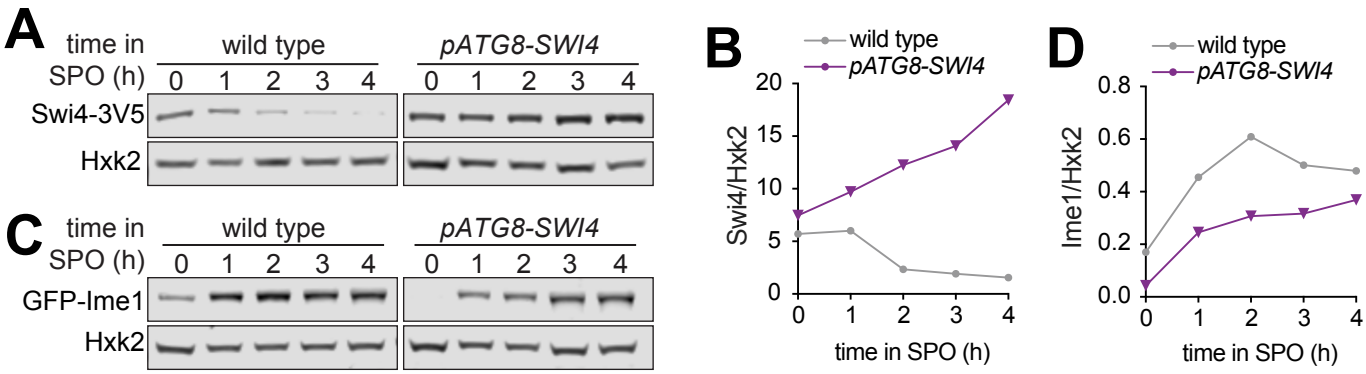

Figure 2 Supplement

Su et al_Figure S2

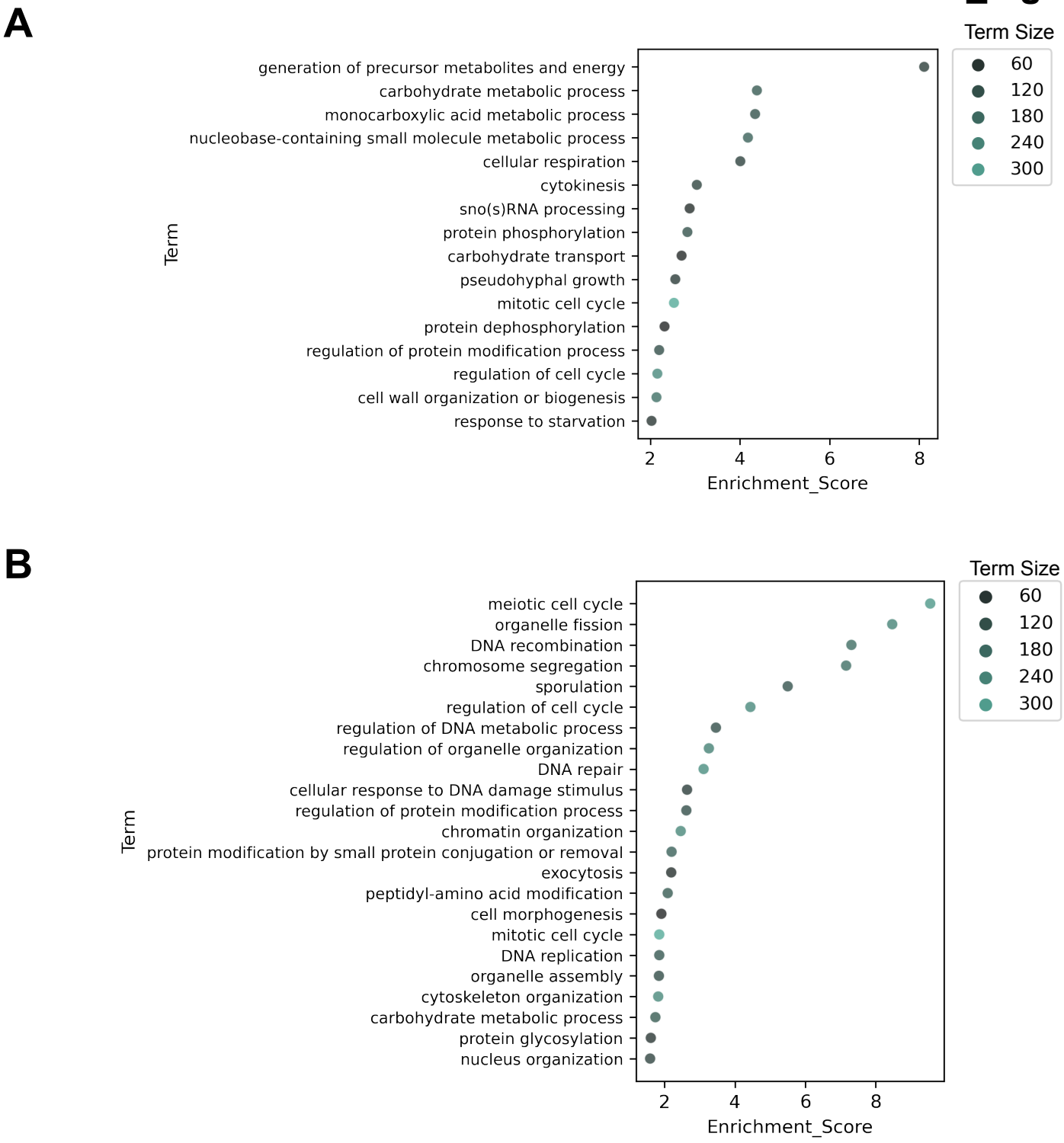

Figure 4 Supplement

Su et al_Figure S4

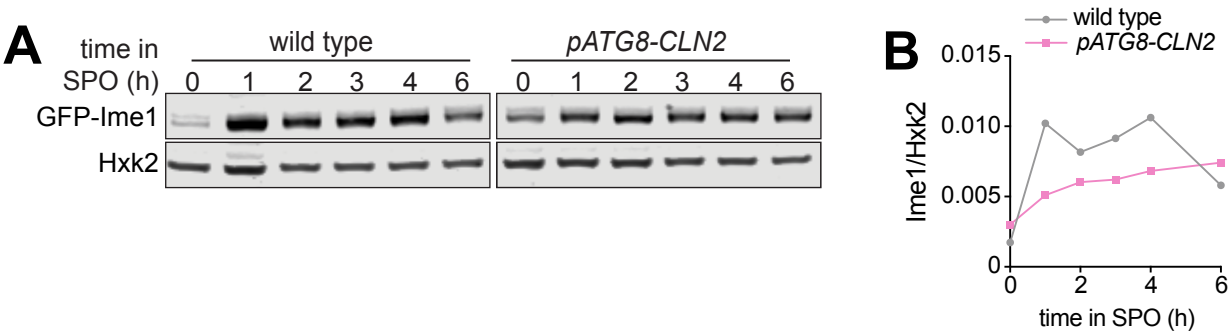

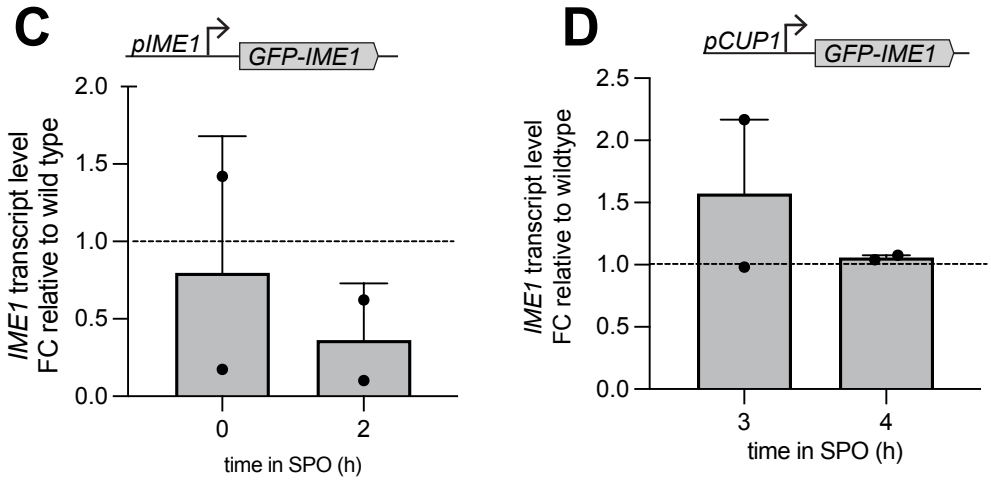

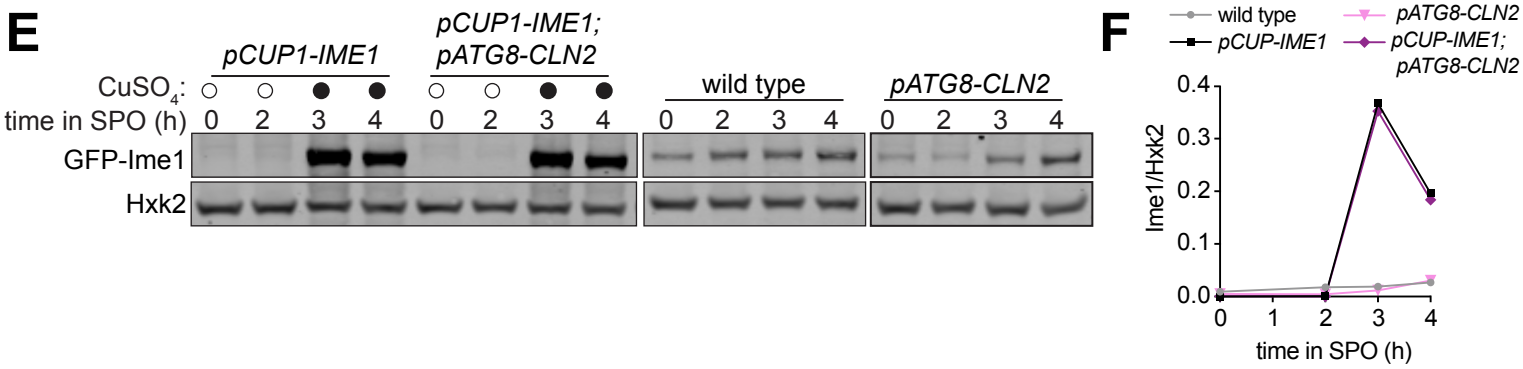

Figure 5 Supplement

Su et al_Figure S5

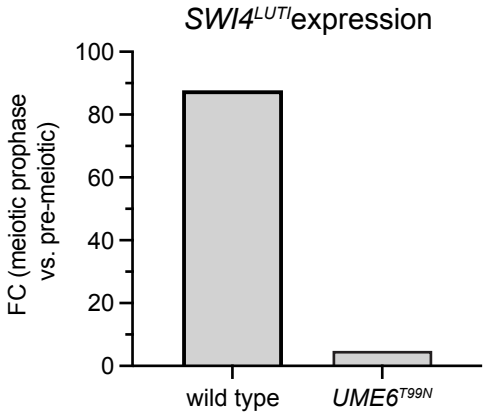

Figure 6 Supplement
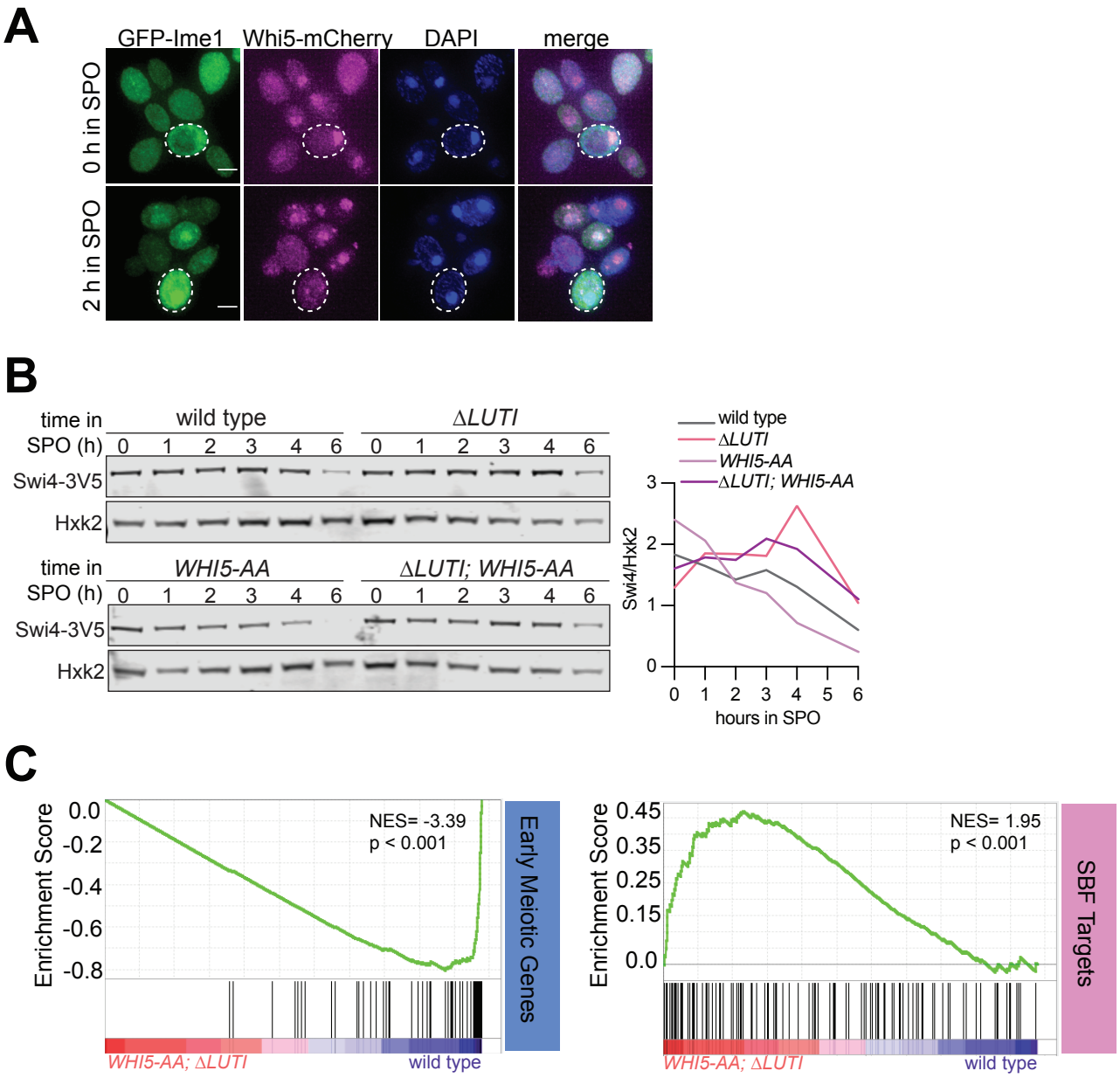
Su et al_Figure S6